Spectral Analysis of Integrated F-Center Feedback Dosimeter

by

Daniel Schumaker

Submitted to the Department of Nuclear Science and Engineering in partial fulfillment of the requirements for the degree of

Bachelor of Nuclear Science and Engineering

at the

Massachusetts Institute of Technology

September 2018

©2018 Daniel C Schumaker. All rights reserved.

The author hereby grants to MIT permission to reproduce and to distribute publicly paper and electronic copies of this thesis document in whole or in part in any medium now known or hereafter created.

Signature of Author: Signature redacted

Department of Nuclear Science and Engineering

May 25, 2018

Certified by: Signature redacted

Michael P Short

Class '42 Career Development Associate Professor of Nuclear Science and Engineering

Accepted by: Signature redacted

Michael P Short

Class '42 Career Development Associate Professor of Nuclear Science and Engineering

Chairman, Committee on Undergraduate Students

MASSACHUSETTS INSTITUTE OF TECHNOLOGY
MAY 02 2019
LIBRARIES
ARCHIVES

Spectral Analysis of Integrated F-Center Feedback Dosimeter

by

Daniel Schumaker

Submitted to the Department of Nuclear Science and Engineering on May 25, 2018 in partial fulfillment of the requirements for the degree of Bachelor of Nuclear Science and Engineering

Abstract

Proton therapy has yet to implement an *in-vivo, real-time, fault-tolerant* integral dosimeter. Proposed in this thesis is a conceptual dosimeter to meet such requirements, relying on the radiation-stimulated production of F-centers in alkali halide salts. F-centers are optically active vacancies in the cation-anion lattice filled with a lone electron. These vacancies cause dimming bands in broad-band illumination of the crystal, and the vacancies increase in number in a proportional fashion to the dose received. The experiment proposed here will serve both to measure the dimming quality of various alkali halide salts as well as their decay rate in the dark at room temperature. Once performed, this experiment will demonstrate the feasibility of correlating dose to a *real-time* color measurement of an implanted alkali halide crystal in a patient undergoing proton radiotherapy. Thus far no such experiments have been performed, however the experimental assembly outlined herein is nearly fully constructed and nearly ready for experimentation upon time of completing this thesis.

Thesis Supervisor: Michael P Short

Title: Class '42 Career Development Associate Professor of Nuclear Science and Engineering

Acknowledgements

The author would like to give special thanks to:

~Si Ci Ong

~Michael P Short

~Cody Andrew Dennett

~Sara Ferry

~Max Carlson

Contents

Chapter 1

Introduction

1.1 Motivation and Objectives

Proton therapy could significantly reduce damage to healthy tissue during cancer treatment. The ion beam used has the key advantage of depositing most of its energy at a depth proportional to the incident beam energy. The path through patient tissue to the tumor is left mostly unharmed, where the majority of the dose is deposited at the very end of the beam trajectory. Compared with traditional x-ray treatment which deposits the majority of its dose at the tissue surface, this would greatly reduce damage to healthy tissue, subsequently reducing treatment-induced secondary tumors.

The basic physics behind proton radiotherapy has been understood for decades. Using a cyclotron, ionized hydrogen is accelerated to the MeV energy range where it is then collimated to a narrow beam that can be focused on a patient's tumor. This beam of protons is slowed primarily through coulomb scattering, where the electromagnetic interaction between the proton and surrounding material's electrons incrementally slows the ion. Since the proton is more massive than the electron, one single collision does not impart considerable momentum to the surrounding matter, therefore initially the proton imparts minimal energy along its path. Once the cumulative coulomb interactions have slowed the ion sufficiently, it no longer possesses enough momentum to travel a great distance without significant interaction with the surrounding material, resulting in an abrupt and large energy transfer over a very short distance (this region is often referred to as the Bragg peak, highlighted in salmon with the label "tumor" in *Figure 1*). This can be seen quantitatively in Figure 1, comparing the evaluated stopping range integral (-dE/dx) from the initial beam energy to zero energy. For more detail on stopping ranges and proton-matter interactions see page 9, Proton Interactions with Matter. For example, consider a tumor centered 40mm deep into a patient's body. The proton deposits its energy in a sharp peak at the tumor location, whereas x-ray therapy deposits the majority of the dose at the tissue surface, imparting only a fraction of the x-ray beam energy to the tumor. This requires multiple x-ray beams from a variety of angles coinciding at the tumor location, while still depositing the majority of x-ray energy inside surface tissue rather than the targeted tumor.

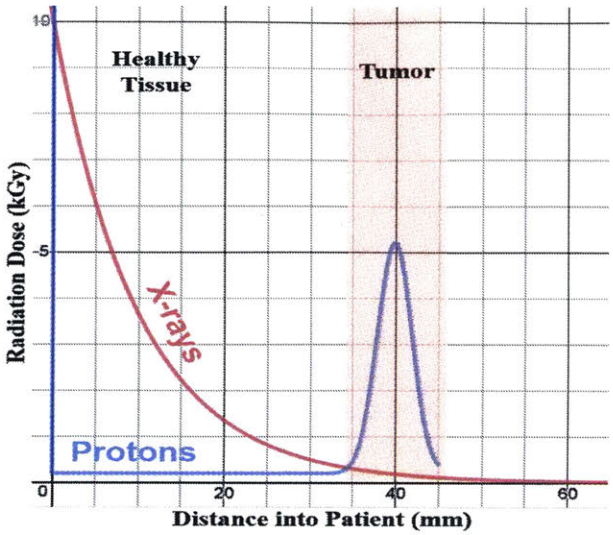

Figure 1: Proton therapy applies the majority of the dose at the cancer site, in contrast with x-ray therapy where the majority of the radiation energy is deposited in healthy surface tissue. Additionally, several more x-ray beams are required to achieve the same tumor-dose as the single proton beam, further increasing healthy tissue damage, and increasing the likelihood of future tumors.

Some obstacles still face proton therapy that inhibit its commercial success, particularly with both measuring dose, and focusing the proton beam in a precise location without the patient's organs moving. This project seeks to remedy both problems in one approach, by using an implanted alkali-halide salt in-situ that can both alert an operator that the tumor has deviated from the beam path and simultaneously measure the radiation dose to the affected area.

The IF²D project (Integrated F-Center Feedback Dosimeter) relies on F-center production, optically active vacancies produced by ionizing radiation that shift the spectral response to white light with dose to the crystal. By illuminating an alkali-halide crystal with white light and measuring the transmitted frequencies in *real-time*, an implanted chip gives near-instant feedback to operating controls. If the dose rate is too low – for example: a result of improper alignment with affected tissue – a cutoff signal can be sent instantly to the beam port. If the dose rate is too high, then the beam intensity can be reduced. Through successive technological refinement, this project potentially could lead to a marketable, affordable technology for quantifying radiation dose to healthy tissue and tumors, removing decades of guesswork and uncertainty. Furthermore, it could greatly increase the feasibility of safely executing proton radiotherapy and minimizing healthy tissue damage. This technology could not only save lives in the short term, but also prevent future illnesses that can often arise from cancer treatment, allowing peace of mind for those who have undergone the trials of cancer therapy.

Chapter 2

Background

2.1 Proton Interactions with Matter

Protons are elementary particles known most for their role in defining the nucleus of an atom. The periodic table of elements is organized according to the number of protons, Z, in a given nucleus, and many of an element's chemical properties are closely correlated with Z. However, in the case of radiotherapy, a proton beam is stream of unbound protons, or more simply a collimated stream of ionized hydrogen. Each proton possesses a single unit of elementary charge, +1, or 1.602×10^{-19} Coulombs, equivalent to but opposite the charge of a single electron (-1). Being charged, these particles interact primarily through the coulomb force, a subset of the electromagnetic force, second strongest of the four fundamental interactions. As such they dissipate energy rather quickly in matter due to the strength of their interaction. One can characterize the energy dissipation rate using the *Bethe Formula* (Equation 1 and Equation 2) listed below which gives the stopping power (-dE/dx) of a particle through a material, where v and ez are the velocity and charge of the primary particle, N and Z are the number density and atomic number of the absorber atoms, m_0 is the electron rest mass, and e is the electronic charge. The expression for B (Equation 2) is largely a general-relativistic correction and changes slowly with particle energy for most primary particles, and can be substituted as $1/v^2$ for particles at non-relativistic energies [1].

Equation 1

$$-\frac{dE}{dx} = \frac{4\pi e^4 z^2}{m_0 v^2} NB$$

Equation 2

$$B \equiv Z\left[ln\frac{2m_0v^2}{I} - ln\left(1-\frac{v^2}{c^2}\right) - \frac{v^2}{c^2}\right]$$

Plotting the stopping power with respect to the particle distance in the material yields what is formally known as the *Bragg Curve* shown in Figure 2. An approximate snapshot of the physics at play is captured in this diagram. At the start of the beam path (surface of absorbing material) the charged particles possess a high momentum and velocity resulting in reduced interaction time between each unit of the surrounding material. These interactions impart minimal energy until the particle is sufficiently slowed that the cumulative interactions along this path dominate in a very short length right at the peak of the curve in Figure 2, often referred to as the *Bragg Peak*. Here the particle deposits the majority of its energy and then is fully stopped. The path along which energy is deposited in surrounding material is where damage occurs, with more energy deposition indicating greater damage. In terms of human tissue, the region in which the radiation deposits the most energy is the region in which the most free-radicals are produced and thus the region of most damage to DNA occurs, both to healthy tissue and tumors.

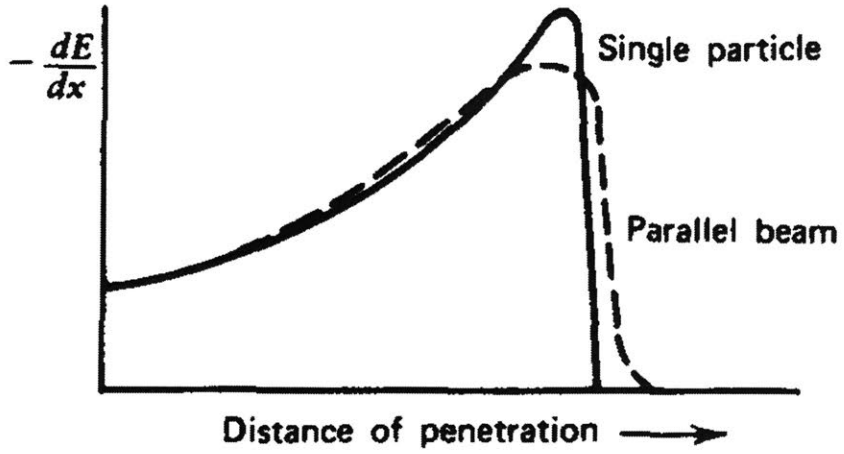

Figure 2: Sketch of charged particle stopping power with depth into target. Protons exhibit this pattern of behavior when transiting through material, remarkable for its sharp peak at the end of the particle trajectory where the most energy is dissipated within the smallest distance, ideal for targeting tumors at the end of the beam path. Refer to chapter 2 in Knoll for more information about radiation interactions with matter [1].

Definition of Dose:

The unit of choice for quantifying radiation damage in this report is Gray or Gy. Gray is defined as one joule of energy deposited into one kilogram of matter. This unit is useful because it captures the end result of the elementary physics at play when radiation interacts with matter, where ultimately the damage arises from deposition of energy from the incident radiation into the surrounding material.

Other archaic units such as Rad and Rem are not formally used in this report, though a brief description is given:

- One rad is equivalent to $1/100^{th}$ of a Gray, and has since been replaced by Gray as the SI unit for radiation damage.
- Rem is a weighted unit, taking the energy deposited in Rad and multiplying it by a 'tissue-weighting factor' which captures approximately how sensitive a given irradiated organ is to radiation damage. For instance, the gonads are highly susceptible to radiation damage because of the extremely frequent cell divisions in that location and thus receive a high weighing factor, whereas skin does not require such delicate chemistry and frequent cell division and receives a low tissue weighting factor as a result.

Both Rem and Rad are outdated units that are formally discouraged in chapter 5.2 of the style guide for the U.S. National Institute of Standards and Technology [2].

2.2 Solid State Physics: F-Center and Other Point Defects

Point defects are a wide variety of ion configurations within a crystal lattice that disrupt the crystalline cation-anion lattice symmetry. A small subset of these defects are discussed below, with emphasis on the F-center.

F-Center:

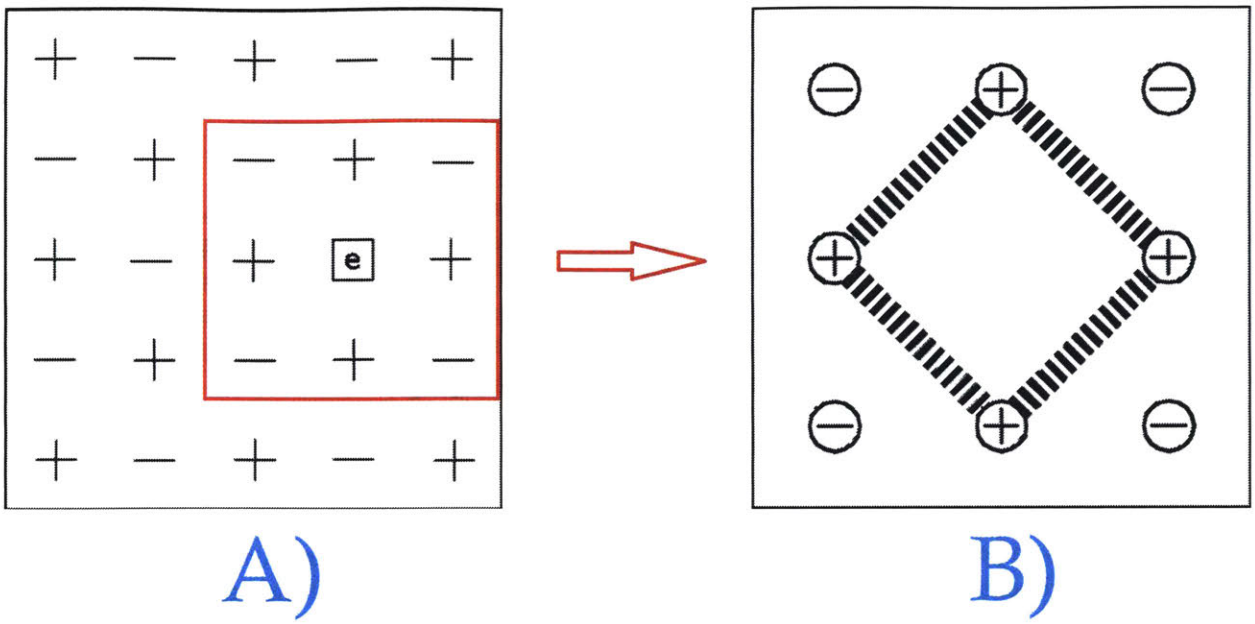

Figure 3: Left (A): A single anion vacancy is filled with a single electron. This vacancy substitution is known as an F-center. Right (B): The single electron is bound in center position by the four surrounding cations (6 cations when considering full 3D geometry), and thus this center is capable of interacting strongly with a photon with frequency near it's natural harmonic modes. This give rise to specific narrow frequency bands that are absorbed preferentially in crystals containing numerous f-centers, and can result in coloration of the crystal upon formation of a significant enough of F-centers [3, 4].

Figure 3 shows a basic theoretical schematic of an F-center in 2 spatial dimensions. The F-center is an optically-active single anion vacancy substituted with a single electron, bound in place by the neighboring 4 cations, or 6 cations when consider full 3-dimensional geometry. With an approximately cubic-shaped potential-well in 3D, the bound electron, much like a string of an instrument, has a fundamental harmonic mode. This mode can couple to that of a photon with frequency near enough such that the electron can capture the photon, creating dimming bands observed in the macroscopic view of the crystal [3, 4, 5, 6, 7, 8, 9, 10, 11, 12].

In almost all alkali-halide salts the F-center preferentially absorbs a narrow color band in the visible spectrum. Some alkali-halide salts have F-center color bands just outside the visible spectrum, for instance CsI has an F-band at 785nm [5], in the infrared region, and LiF has a F-band at 247nm [10], in the ultraviolet region. Alkali-halides with F-bands in the visible spectrum are of principle interest for the purposes of *in-vivo* dosimetry, as visible-range optics are readily miniaturized into chip-scale devices such as an implantable dosimeter.

F-centers can easily be formed by bombarding an alkali-halide crystal with radiation [8]. X-rays were among the earliest studied forms of radiation used to produce color centers in alkali-halide salts [13]. X-ray intensity decays exponentially through material, and can be modelled using Equation 3, where $I(x,\lambda)$ is the intensity of the x-ray beam of monochromatic wavelength λ at depth x in a material with absorption coefficient μ and $J_0(\lambda)$ is the initial beam intensity of monochromatic wavelength λ. It is easy to model the quantity of F-centers produced by x-rays under the assumption that their decay is on a timescale orders of magnitude greater than their formation. Mador and Wallis give the governing 1-dimensional differential equation under this assumption, Equation 4, where $n_F(x)$ is the number of F-

centers at depth x, and I(x) is the beam intensity, time is t, and a is an arbitrary constant [8]. As seen, the rate of F-center formation is directly proportional to the x-ray beam intensity in a given region.

Equation 3
$$I(x,\lambda) = J_0(\lambda)e^{-\mu x}$$

Equation 4
$$\frac{dn_F(x)}{dt} = -a\frac{dI(x)}{dx}$$

F-center production obeys similar but distinct equations for proton irradiation, where the beam intensity is no longer a decaying exponential like that in Equation 3, but rather a *Bragg Curve*. The F-center concentration can be modelled using Dexter's version of the Smakula formula (Equation 5), where $n_f(x)$ is the number of f-centers per m^3, x the range of protons, n the refractive index of the alkali-halide, f the oscillator strength of the F-band (≈0.8), A the peak optical density (or absorbance $\ln[I_0/I]$) of the F-band, and W the full-width at half-maximum of the F-band in eV [14]:

Equation 5
$$n_F(x) = 2.01\times10^{21}\frac{n}{(n^2+2)^2}\frac{AW}{fx}$$

Equation 5 is vital to quantifying the F-center production under proton irradiation for this experiment. It is important to note this equation does not capture the differential creation of F-centers with respect to time, beam energy and intensity. Rather this equation is the solution to such equations in context of a full beam profile, the *Bragg Curve* for each irradiation performed. For proton RT, irradiations are designed and planned using a discretized version of the stopping power with respect to proton energy and integrated in discrete fashion to generate a monte-carlo predicted *Bragg Curve*. From this data the depth, x, is determined for Equation 5 before irradiations are performed. Additionally, the index of refraction, n, and oscillator strength, f, are known prior to irradiation. The independent variables for these irradiations are simply the peak optical density, A, and full-width at half-maximum, W, of the spectral band. Upon measurement of these two quantities, an accurate prediction of the F-center density can be performed.

Other Point-Defects

Point defects are a broad class of atomic-scale impurities in a given crystalline lattice. Any disruption of the cation-anion parity in the lattice is a point defect. Many names have been given to a variety of different defect types, with a surprising lack of a centralized description of all of them in literature. Discussed here are just a small subset of defects relevant to this topic, including [4]:

a. F-center
b. F'-center
c. V-center
d. α(±)-center
e. U-center

As seen and discussed, the F-center is a single anion vacancy substituted with an electron, with a half-life on the order of hours, and are of principle interest for this project. Shorter lived is the F'-center, which generally decay with a half-life on the order of seconds, where two electrons have been trapped in a single anion vacancy. Some puzzlement surrounds the nature of binding the two electrons in a single potential well. For most crystalline hosts, such as KCl, NaCl, and KBr, the potential well of a single anion vacancy is significant enough to trap two electrons, but for others such as NaBr, NaI, and LiCl the lattice polarization appears to be the major factor binding electrons into the F'-center [15]. Regardless, it has been found F'-centers are more stable and longer lived at cryogenic temperatures, but such temperatures are not viable for the purposes of this experiment [9].

The V-center is a theoretical self-trapped hole, where a hole from an electron-hole pair creation event has migrated to fill a single cation vacancy. This center is not of principle investigation for this project.

Anion and cation vacancies are referred to as α^--centers and α^+-centers respectively, and are simple vacancies where an ion has left its location in the lattice and surrounding ions have migrated position slightly to compensate.

Lastly, the U-center is an important consideration for future experimentation. The U-center is a hydrogen-filled anion vacancy, and will arise in greater frequency under proton irradiation than any other form of radiation for a given material as the proton beam is essentially ionized hydrogen gas. U-centers in Alkali-Halide crystals are known to give rise to triply degenerate localized vibrational modes that are infrared-active [16]. This eliminates the U-center from study for this project given that both the photospectrometer used for this project cannot read in the infrared range and that optical-range photon interactions are desired for the IF^{2}D project for chip-scale dosimetry manufacturing. Regardless of these factors, the U-center nonetheless warrants future investigation for its potential role in proton dosimetry for larger-scale applications.

Figure 4 gives a simple theoretical schematic of these centers.

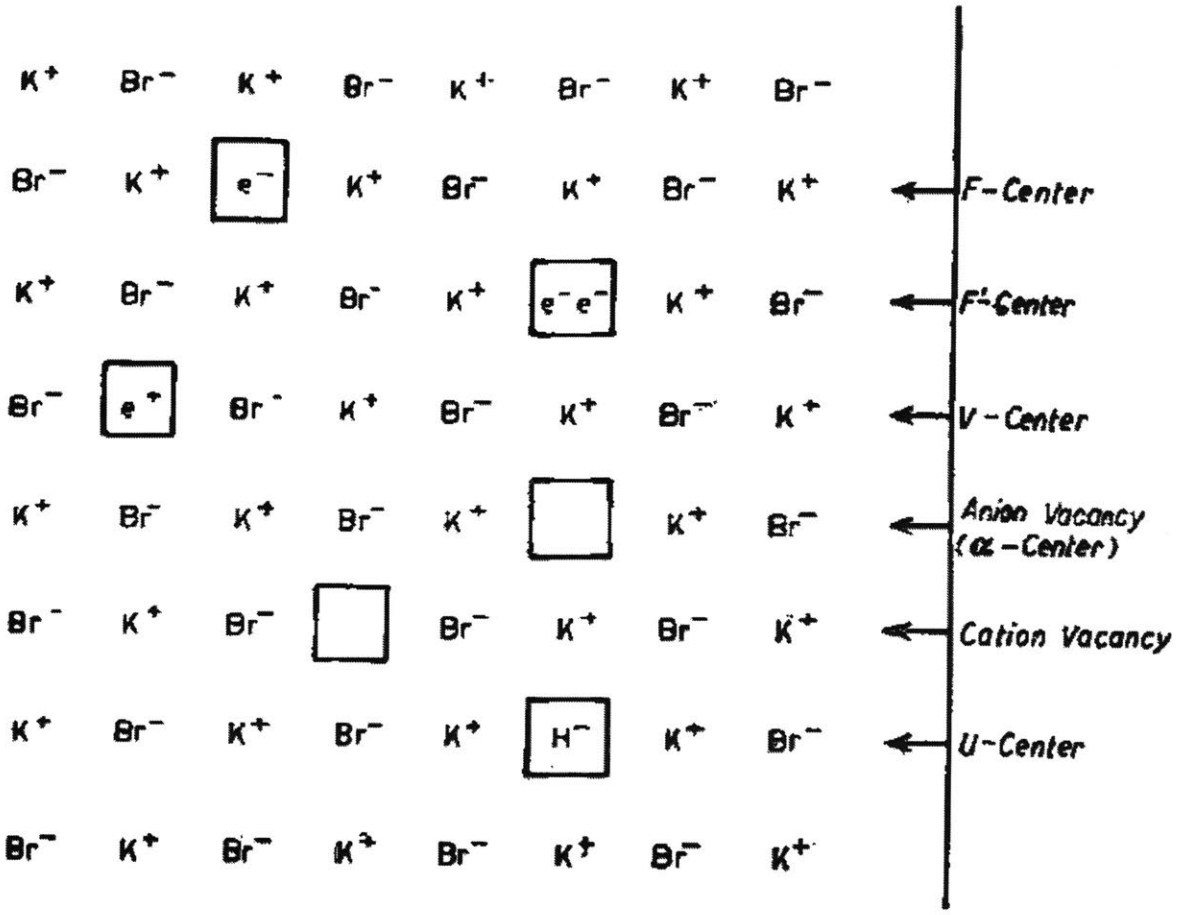

Figure 4: H. Pick's Summary of different color centers in alkali halide crystals, with an example Potassium Bromide (KBr) lattice [4]. The F-center is a single anion vacancy filled with a single electron. The shorter lived F'-center is pictured directly below with two electrons filling an anion position, generally more stable at liquid nitrogen temperatures. The V-center depicted is a theoretical self-trapped hole, not to be confused with a positron filled vacancy. Anion and cation vacancies are shown, referred to as α-centers (± with respect to the charge of the vacancy). Lastly the U-Center is shown as a hydrogen-replacement in an anion vacancy. This center will be more common under irradiation of a proton beam with respect to other forms of ionizing radiation.

2.3 Radiation Therapy

Radiotherapy (RT) has been a crucial method of treating cancer for over a century. Starting only a handful of years after Roentgen first proposed the existence of the x-ray in 1896, it was found repeat exposures of tumors to x-rays could cure the disease [17]. By the start of the 20th century, however, it became clear x-rays also cause damage to healthy tissue as well as future cancerous growths in patients, during which time many early recipients of x-ray therapy found themselves with Leukemia and other related illnesses [17, 18]. It was found that photon radiation deposits dose in a given material in an exponentially decaying manner with respect to depth [1], indicating the majority of x-ray dose to a patient's tumor is deposited in the surface of the patient's skin rather than in the interior of the patient's body (see *Figure 1*).

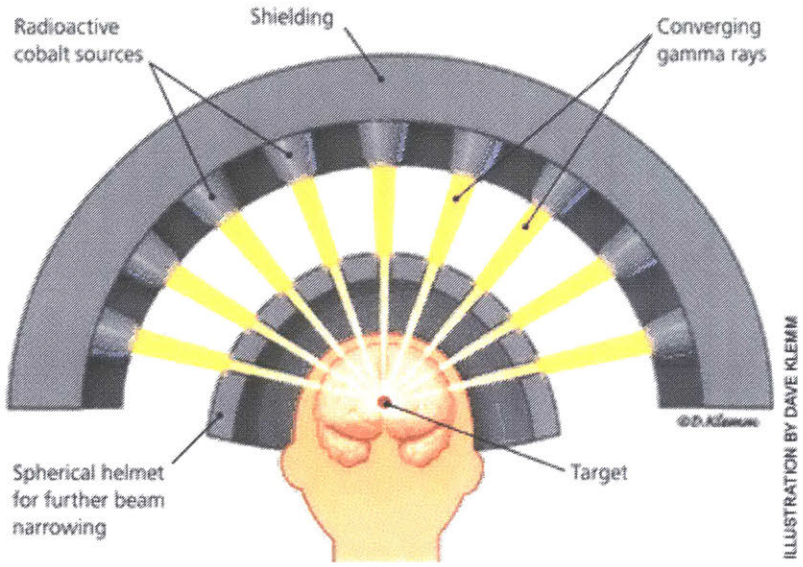

Figure 5: Multiple x-ray/gamma-ray 'knives' are focused on the tumor for stereotactic x-ray therapy [19]. *This leaves the majority of the radiation dose at the patient surface and requires expensive machinery to focus multiple beams. Proton therapy only relies on a single beam with the majority of the radiation dose concentrated at the tumor.*

To avoid detrimental effects from this behavior, current forms of x-ray therapy generally use multiple "knives" of x-rays or gamma rays focused into coincidence at the patient's tumor. *Figure 5* shows the geometry of x-ray "knives" in a standard stereotactic setup, which is a subset of x-ray RT that is generally applied for patients with small tumors or functional abnormalities [17]. Outside the brain, stereotactic radiosurgery requires immobilization of the patient using fixtures and equipment which can then be used for precise targeting of tumors. This allows the large surface dose inherent to this method to be distributed more evenly and with less intensity along the patient's skin, helping to mitigate healthy tissue damage. While this technique is valuable for its low cost-to-efficacy ratio and its long history of successful implementation, the majority of the radiation never reaches the patient's tumor. Other forms of radiotherapy have been proposed because of this inherent flaw, including but not limited to brachytherapy, neutron therapy, and proton therapy. This study focuses on dosimetry for the purposes of proton therapy owing to its unique dose profile.

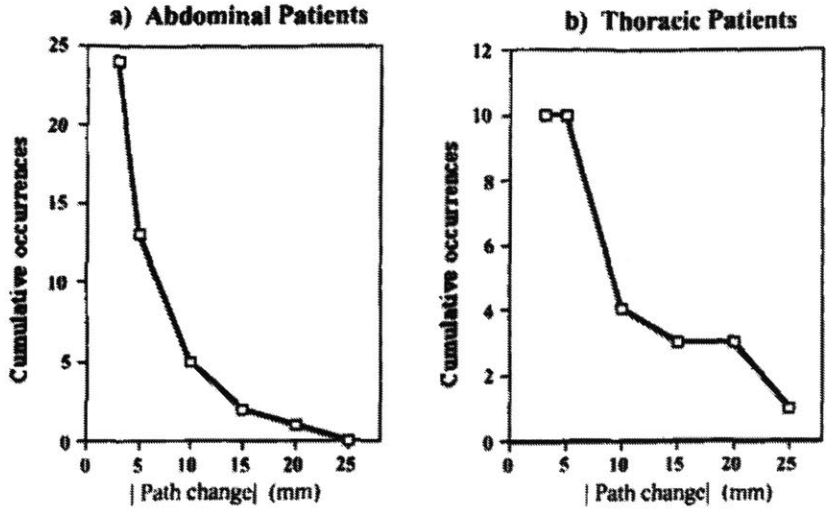

Figure 6: Patient breathing increases uncertainty in tumor location during RT, with deviations in position up to 25mm found in patients with abdominal (a) and thoracic (b) tumors [20]. More precisely-targeting RT techniques such as proton therapy are more susceptible to off-target irradiation because the dose location is smaller and therefore less likely to intercept a tumor when off-focus during nominal movement.

Proton RT has been used in treatment for over two decades, its popularity owing to the dose of the beam being deposited inside the patient at the tumor rather than at the surface of the skin (*Figure 1*). This makes proton therapy ideal for the treatment of cancers where there is an urgent need to spare healthy surrounding tissue, for instance cancers in children, the eye, base of the skull, the prostate, and other sensitive organs [21]. However, this therapy technique has not gained widespread commercial success owing to numerous key difficulties. The cyclotrons necessary to accelerate protons to hundreds of MeV in energy are both considerably expensive and large, making their cost-to-efficacy ratio rather high despite the superior targeting of tumors achieved with these devices [22]. For instance, in 2008 Chui estimated the average cost of a proton therapy facility to be between $120 to $180 million, and with an average size of a football field [21]. Additionally, nominal movement of patient's internal organs, even when the patient appears perfectly still, can increase off-target irradiation of the patient's healthy tissue, ironically due to the high precision of this RT technique [20].

Figure 6 shows how patient breathing can disrupt the calculated path length an RT beam must travel to reach the tumor. Computerized tomography (CT) scans were used to plot an RT beam path when patients were exhaling and separate plots for when CT scans were performed while the patients were inhaling. The difference in calculated RT path lengths between inhaling and exhaling are charted numerically above in Figure 6, showing deviations multiple centimeters long at most severe. In addition to the demonstrated organ movement, the apparatuses used for positioning during RT can have small geometric differences between runs. Further uncertainty is compounded when considering the patient's skin movement with respect to their internal anatomy, affecting the CT scan data used to plot the RT beam path. Further complicating the computer models, the human body is comprised of different organs which absorb radiation differently making it harder to predict the overall trajectory of the RT beam, especially when differently absorbing organs are moving in and out of the beam path during breathing.

Even at most ideal, it is unlikely if not impossible to remove these sources of positional uncertainty, and as such computer models of radiation implantation can only *predict* where the beam reaches during treatment and cannot wholly guarantee the accuracy of the modelled irradiated regions.

As such it is essential some form of direct measurement be performed in-situ to monitor the rate of radiation entering the tumor region, and if possible characterize the energy profile in some way.

2.4 Radiation Dosimetry

The mechanism of radiation dosimetry requires some volume of matter that interacts with an ionizing unit of radiation. Ideally, that volume of matter must interact in some way proportional to the dose deposited in the material, and that interaction must be measured and quantified [1]. This principle has underpinned radiation detection since the inception of the Geiger-Muller detector, one of the earliest forms of counting radiation [23].

Measuring and quantifying radiation can take many forms. For instance, the Geiger-Muller design is optimized for counting ionizations but does not retrieve any information about what energy of radiation has entered the detector and it can be extremely difficult if not impossible to infer which type of radiation has entered the ionization chamber for most setups. On the other end of radiation-counting devices are high-purity Germanium single-crystal detectors which can not only count radiation, but also distinguish the energy of each ionization event with remarkable accuracy. Each type of detector has tradeoffs. For instance, a simple Geiger-muller tube often can register more events under a given amount of radiation than for Germanium semiconductor detectors due to its intrinsic detection efficiency. This makes the Muller tube more ideal for applications where low activities are present and very little time is given to count, and the Germanium detector ideal for detection of specific energies of radiation given plenty of time.

Much like the tradeoffs between Geiger tubes and Germanium detectors, dosimeters for RT vary in capability as well. One detector may be able to measure radiation energies but cannot be implanted in a patient, or another detector may be implanted but cannot be read until after removal from the body. While numerous detectors exist for the purposes of RT, there exists no ideal dosimeter given current technology.

The remainder of this chapter and its organization is based on the *Integrating Radiation Dosimetry* 2015 patent proposal through Massachusetts Institute of Technology [24].

In his 2004 Journal of Physics conference series, C. De Wagter details a formal set of criteria for the ideal proton RT dosimeter in which he notes 8 dosimeter characteristics that serve as a guide for future dosimetry research [25]:

1) Can determine absolute dose (in Gy)
2) Can capture full 3D profile
3) Is orientation independent
4) Dose readout is calibrated and supported by well documented and established data
5) Dose profile in Gy is independent of beam current and energy, ex: For 1 minute of irradiation, 1MeV protons at 2nano-amps will yield the same dose readout as 2MeV protons at 1nano-amp
6) Interpretable readout for both low-density and high-density tissue regions
7) Comprised of non-toxic materials
8) Construction and implementation of dosimeter is within reasonable cost

Proposed here is a set of addenda to further refine Wagter's assertions for the ideal dosimeter:

- *Real-time* feedback that can instantly communicate with beam control systems in case the beam is off-target or can provide refined dose details to inform the controller how to change the beam intensity, energy, or direction.
- *In-vivo* operation such that the dosimeter is directly inside or next to the patient's tumor to monitor all points of interest during treatment.
- Bio-compatible such that the patient's health is not at risk during operation, the dosimeter is easy to implant, and does not contain nuclides such as ^{63}Cu (the most common Copper isotope $\approx$69%, used in electronics and wiring) which can produce neutrons upon bombardment by protons (see Figure 7), by extension creating other forms of harmful radiation inside of the patient.
- Fault tolerant such that when the electronics for the dosimeter fail, all or at least some information can still be gathered from the dosimeter.

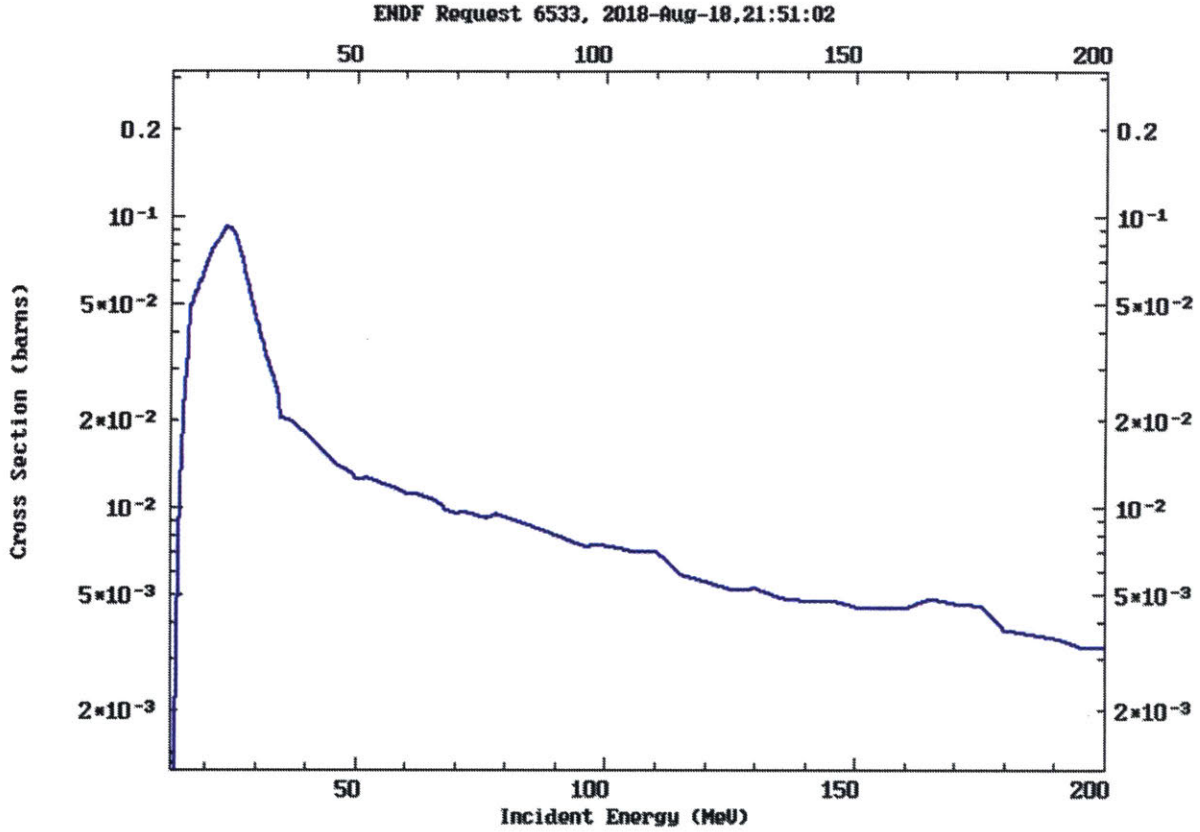

Figure 7: ^{63}Cu (p,2n) reaction cross section [26]. Cross sections are a geometric interpretation of the effective size of a nucleus for a given reaction, and can be thought of as a proportional proxy for the probability of the listed nuclear reaction. In this reaction, a single proton reaches a ^{63}Cu nucleus and is absorbed followed near-instantly by emission of two neutrons which can then induce further radiation production inside of a patient. This makes copper wiring and traditional electronics dangerous when irradiated with protons inside a patient. Dosimeters for proton RT must avoid use of copper.

Several different dosimeters currently in use or are being considered for use in proton RT dosimetry are discussed below. These include:

Ex-vivo techniques:

a) Thermoluminescent dosimetry
b) Monte Carlo Simulations
c) Port Films
d) Electronic portal imaging devices
e) Gel dosimetry
f) Electron Spin resonance spectroscopy

In-vivo techniques:

g) Silicon diodes
h) Scintillation fibers
i) Prompt gamma monitoring
j) PET scans
k) MOSFET dosimeters

2.4-a Thermoluminescent Dosimetry

Thermoluminescent dosimeters (TLDs) are one of the most often implemented dosimeters for RT and function in a manner that is distinct yet similar to the dosimeter proposed for this report. TLDs are often simple crystals, often alkali-halides, such as Lithium-Fluoride (LiF) and Calcium-Fluoride (CaF), though recent research indicates TLD behavior is possible for exotic compounds such as opal nanocrystals [27]. These crystals build up point-defects, or atomic-level impurities in the crystal lattice, that store energy deposited by radiation. While many defects vanish quickly and cannot be measured, long lasting defects with half-lives ranging from hours or days and up to 80yr can be measured by heating the crystal once RT is complete. Heating the crystal produces luminescence, the product of releasing the stored energy in these point defects [3].

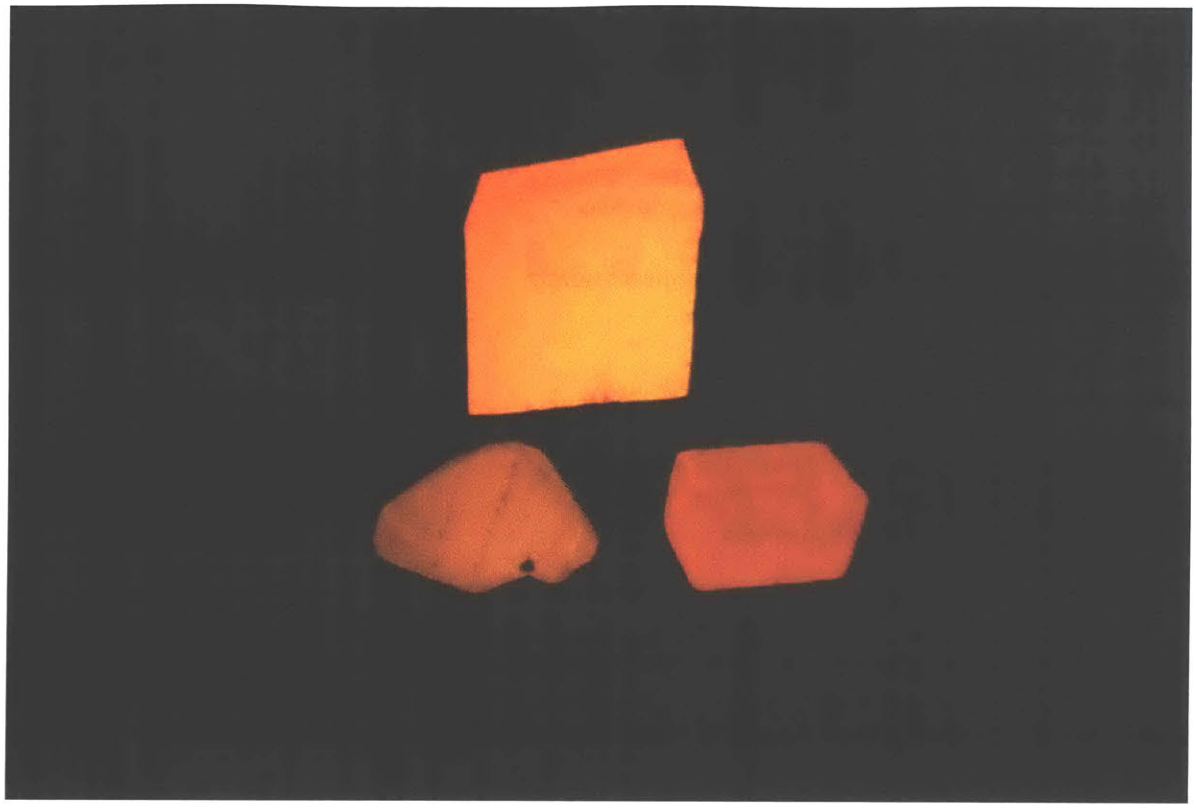

Figure 8: Thermoluminescence at room temperature after 1MGy x-ray dose in various alkali halides [28]

Point defects within a TLD are the result of ionization within the crystal that in turn occasionally result in electron-hole pairs that are boosted into the conduction band, as seen in Figure 9 [3]. Often instead of full radiative or thermal de-excitation, these pairs are bound in trap states from defects in the crystal, where the hole trap and electron trap states exist at a sufficient enough band gap such that recombination is not immediate. While some natural migration to the valence band occurs, the states measured for TLD are typically long lived such that their self-quenching rate is negligible. The trap states in a given TLD are chemically designed such that only sufficient thermal excitation can promote an electron back to the conduction band. Upon heating, this excitation allows the electron to recombine with a neighboring hole releasing visible light that is measured and counted for dosimetry. Generally, provided the TLD is functioning properly, the greater the light intensity from a heated thermoluminescent crystal the greater the dose that was delivered to the crystal prior to heating.

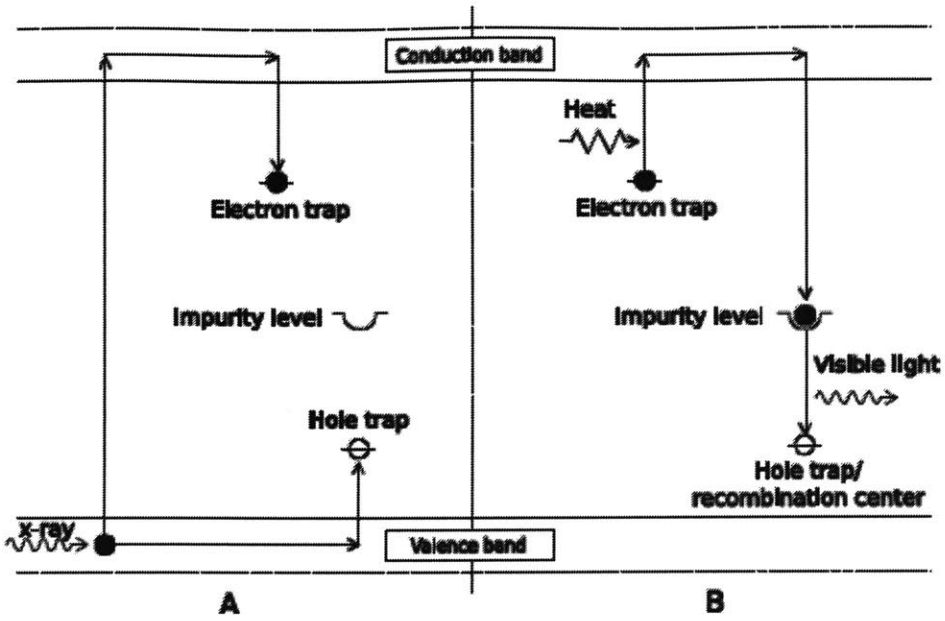

Figure 9: Ionization from irradiation promotes electron-hole pairs into trap states in defects within the crystal [3]. Upon heating of the crystal, the trapped pairs are given the appropriate activation energy to allow for full recombination, releasing visible light that is then counted for dosimetry.

Thermoluminescent dosimetry, while certainly useful, is burdened by key drawbacks. Foremost among these drawbacks is the TLD's lack of *real-time* feedback. Any TLD must be removed from the patient and heated in a purpose-built facility to be measured properly. This means no dose information can be gathered until well after irradiation is complete, making this technology only suitable for verifying monte-carlo predicted doses rather than as a feedback controller for a proton beam. This alone invalidates much of the TLD's potential usefulness for proton RT.

Further complications surround the TLD with respect to limits on locations of applicability and susceptibility to setup error. The former is a result of the TLD requiring removal from patient before dose can be read. This inhibits implantation into a patient's body and narrows the TLD's useful locations to orifices and skin. For instance, TLDs may be placed on a patient's skin near the thyroid since the gland is near enough to the surface of the neck but cannot reliably be directly implanted in deep tissue such as the kidneys or liver [29, 30]. TLDs are prone to setup error. If an operator improperly sets up a TLD for RT, that TLD reading will still be gathered but will be read with far greater uncertainty, further confounding treatment effectiveness estimations [31].

2.4-b Monte Carlo Simulations

Monte Carlo (MC) simulations are strictly theoretical calculations and are not true experimental dosimetry readings. However, they are often used to plan irradiations for any radiotherapy technique. Monte Carlo *dosimetry* simulations are a subset of the broad class of Monte Carlo simulations which are iterative methods that rely on repeated stochastic sampling from a given distribution or set of distributions. While there is no rigorous, centralized definition of the Monte Carlo method that does not exclude key valid examples, Harrison nevertheless gives a crucial set of characteristics which can serve as an approximate definition [32]:

- Model a system as a (series of) probability density functions (PDFs)
- Iteratively sample from PDFs
- Track results and statistics of interest

A relevant example of a Monte Carlo simulation for approximating the depth of proton-penetrance for proton RT is as follows:

Setup: A tumor location is known to be at a depth starting at 55mm and ending at 145mm past the patient's skin. The dose in Gy required to be directly delivered to the tumor is calculated already given biological considerations for what damage is required for tumor-lethality (expressed in percent, where 100% is tumor lethal dose). The energy and intensity of the proton beam has been approximately calculated in a range of a few MeV and some given flux. Simulation is required to check the first-order calculations, by tracking a beam of particles, one particle at a time, at a given starting energy and stochastically estimating energy loss per unit distance travelled through the patient's body. This yields the predicted number of protons and their depth distribution given the stochastic nature of their slowing, appearing in data as an effective *Bragg Curve.*

The simulation proceeds in single time-steps, where during each step the particle's initial position, direction, and energy are used to calculate the updated position, direction, and energy for the next time step. Each time step proceeds as follows:

1. Particle has initial velocity, $\vec{v}_0 = \langle v_x, v_y, v_z \rangle$ (by extension some initial energy E_0, and direction $\vec{\theta}_0 = \langle \emptyset, \varphi \rangle$) and position $\vec{X}_0 = \langle x, y, z \rangle$.
2. Using an interaction probability distribution and tabulated values for Equation 1 and Equation 2 in section 2.1, the energy loss for the particle is calculated over the distance travelled in the present time step, given the type of material it is travelling through along that path.
3. The particle is now assumed to have travelled along a given path vector based on the initial position and velocity. The position for the start of the next time step is saved.
4. The particle is now assumed to have lost energy along the path. The velocity for the start of the next time step is saved.
5. Position and velocity (by extension energy and angle) calculated in steps 3 and 4 replace the current position and velocity and are considered the initial conditions for the next time step.
6. Calculations for current timestep complete, return to step 1 for next timestep.

Upon simulation of enough particle tracks, a curve much like a *Bragg Curve* can be produced, where instead of energy loss per path length (-dE/dx) on the y-axis there is now particle count of particle tracks ending at a given depth x. Given that protons deposit their respective majority dose near the end of their path, this simulated curve can act as proxy for redundantly verifying the location of the *Bragg Peak* after the complicated geometry and density distributions of the patient's body (which are often not captured in first order depth estimates) are considered and rendered in the simulation.

Such a simulation could produce a curve similar to that seen in Figure 10, where a patient is to undergo intensity-modulated radiation therapy (IMRT), a common way to implement RT with proton beams. In IMRT the patient is first subjected to the initial round of irradiation, noted by the *Pristine Peak.* A successive series of lower dose and energy irradiations are performed to form a cumulative dose shown in red in Figure 10. This spread the peak dose over a broader range to target tumors wider than the width of a single *Bragg Peak.* It is important to note this curve was not produced by the exact same monte-carlo method described above which tracks particle track *end positions.* Instead the methods used to produce these curves track information about *energy deposition* along the particle path. End positions were used as an example for simplicity, noting that more refined techniques of information tracking exist in Monte Carlo methods used for dosimetry today [33, 34, 35, 36, 37].

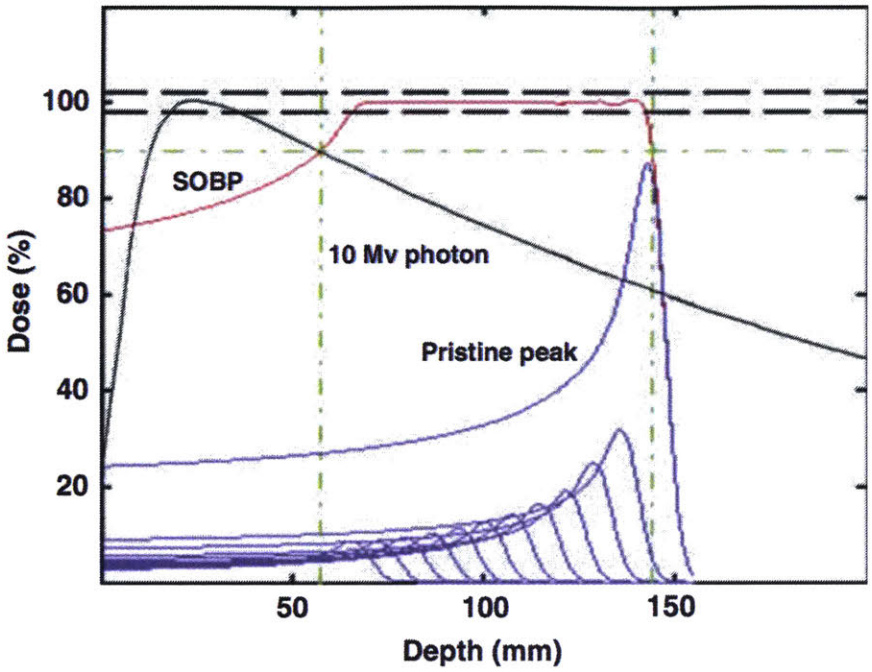

Figure 10: Intensity Modulated Proton Beam Therapy (IMRT) Bragg Curves – multiple irradiations of successively lower current and energy are performed to create a flat integral dose profile for the tumor region. The peaks can be generated using the Monte Carlo technique [38].

Again, it is crucial to note Monte Carlo simulations are not a true dosimetry technique and are strictly theoretical *predictions*. The simulation accuracy is dependent on how precisely the patient's tissue is modelled, how refined the lookup tables for probability of interaction and energy loss characteristics, and how well these models match with reality. Additionally, these computations are resource intensive and often require a supercomputer to run in a reasonable time, increasing cost per evaluation of dose. While Monte Carlo simulations are improving continually with both improved nuclear data collection and development of superior computers which can manage increasingly complex simulations, they still are prone to uncertainty and potential user error during setup. Coupled with the lack of physical measurement and lack of *real-time* feedback, this technique is not ideal as a singular method for determining dose. It is, however vital for predicting a treatment course before irradiation and can be used in conjunction with dosimeters to provide confidence in a modelled and performed RT treatment.

2.4-c Port Films

Port films are purpose-made sheets of film, similar to film used in antiquated cameras, that are placed behind the patient with respect to the radiation stream. The patient is irradiated through 'ports' which are areas of the patient's external body where the beam is aimed during RT. The beam passes through the patient and some exit current is still left that traverses to the port film outside the patient's body. The radiation interacts with the film much like light interacts with film in cameras, creating an 'image' of the radiation exit profile, where areas of more intense irradiation are more saturated [39].

Port films are limited to post-irradiation dosimetry and cannot be used for *real-time* feedback. Additionally, they are used ex-vivo traditionally and cannot be implanted in a reasonable fashion. They are however, passive dosimeters which do not require electronics to run and their dose readout is not compromised by system failure during irradiation. These attributes limit port film technology to passive ex-vivo exit-dose verification at best, and are not particularly suitable for the purposes of proton RT.

2.4-d Electronic Portal Imaging Devices

Electronic portal imaging devices (EPIDs) share similar functionality to the traditional port film, but without the need for development of film as the images are digital. Much like port films, EPIDs are used to check whether the radiation beam is functioning as intended. Perhaps the most notable use of EPIDs is in dental x-ray equipment, where the EPID can read and produce an image from an x-ray almost instantly. Their rapid resolution allows for adaptation for on-line use [40]. Again, like port films, this technology cannot be used for a direct measurement of the radiation dose at a tumor site, and this technology has been almost exclusively developed for x-ray irradiation rather than proton therapy.

2.4-e Gel Dosimetry

Gel dosimetry, as the name implies, relies on gelatin-rich water with radiation-interactive compounds intermixed such that incident radiation causes ionization of the interacting species and induces visible structural change of the gel model along the radiation path. Other techniques rely on small monomers capable of rapidly combining into larger polymers when ionized via incident radiation [41].

This technique has the key advantage of total experimental 3D resolution [42]. When prepared properly, the gel is of perfectly homogenous composition such that any incident radiation interacts as it would in any other volume element of the gel. Examples of property changes in gel upon irradiation include color change, opacity change, or other chemical changes that can be read in 3D. This technique has the additional advantage of using biological or nearly-biological compounds to interact with radiation, negating need for tissue equivalence factors that compound uncertainty. Instead it can be assumed the radiation interacts with the gel in a fashion almost identical to an actual patient.

Disadvantages of this technique include lack of *real-time* feedback and an approximately week-long preparation period for designing and molding the gel. Reading the 3D information from gel dosimeter takes hours at minimum, eliminating any possibility for use in *real-time in-vivo* applications. This technique is best for attempting a proposed radiation treatment on a dummy-patient (seen in Figure 11) comprised of gel prior to RT for the patient, ensuring the treatment proceeds accordingly or needs adjustment.

Figure 11: Two different gel dosimeters, initially transparent then irradiated. The regions of color and opacity change mark the region of irradiation [43].

2.4-f Electron Spin-Resonance Spectroscopy

Electron Spin-Resonance Spectroscopy (ESRS) is a technique used for quantifying radiation dose already delivered to tissue after an unknown or unmeasured amount of radiation has entered a subject. Long lived electron spin-resonances have been known to exist in tissue after irradiation, particularly in bones, fingernails, and teeth [44]. These resonances can be measured and correlated with the initial dose to the subject.

This technique has been used in medical physics, but its application has also been noted elsewhere such as in determining the extent of irradiation to food, as well as use for determining which individuals are in most need of treatment after a mass-exposure incident [45, 46, 44]. While this technique is essentially *in-vivo*, it is not ideal for measuring dose delivered to a tumor. As mentioned, ESRS is most often used on hard tissue such as bones, fingernails, and teeth, and is not as effective with soft tissue. Additionally, ESRS was developed as a post-irradiation technique, and it is extremely difficult to target a localized region such as a tumor during irradiation. Dose information is not localized except for perhaps bone and other hard tissue, and this technique is subsequently better suited for full-body exposure or localized exposure to bone or hard tissue. As such, this is not a reliable *in-vivo* and *real-time* technique for proton RT.

2.4-g Silicon Diodes

Diodes are semiconductors with directional current whose flow is in a near binary on-off state depending on if the diode is subject to a voltage above or below the threshold for which current rises dramatically (refer to Ch. 11 for more information about semiconductors and their respective types [1]). Most commonly, diodes used for radiation dosimetry are of P-type [47].

In Figure 12, a simple schematic of radiation detection using a semiconductor is given. Upon impingement of ionizing radiation through the detector, electron-hole pairs are created that migrate to their respective ends of the detector based on the bias voltage. This creates a measurable current that can be read under a fixed voltage for a constant dose rate. Alternatively, the forward voltage can be read to correlate to received radiation dose in leu of current.

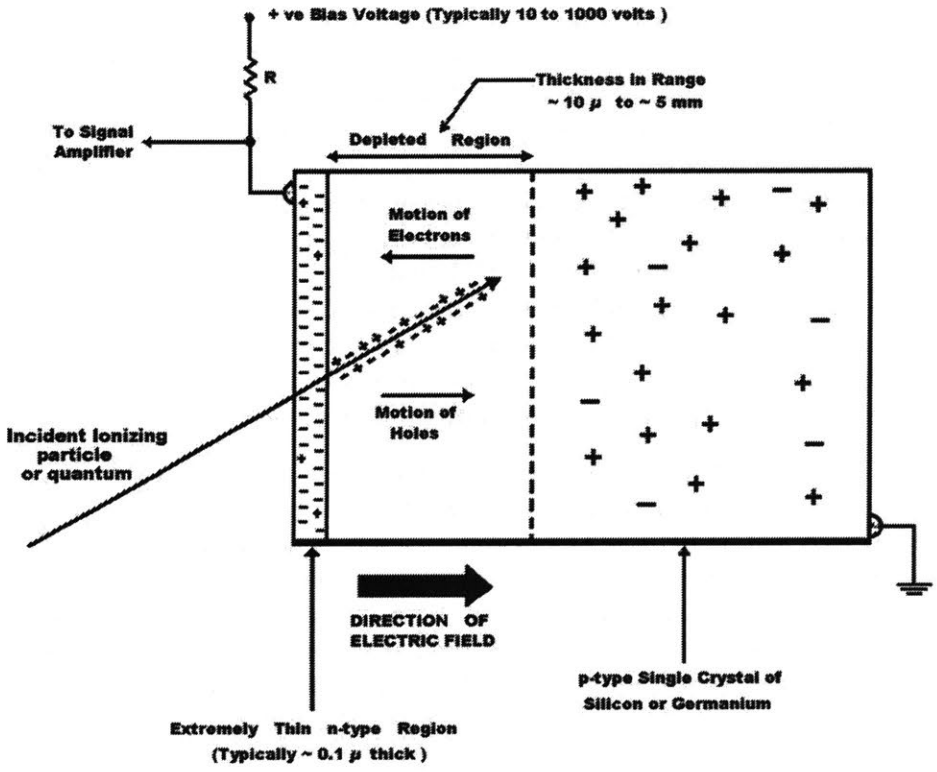

Figure 12: A simple schematic of a silicone diode detector is given. Ionizing radiation induces electron-hole pairs with intensity proportional to the energy deposited in the diode. These pairs migrate creating a signal pulse proportional to the number of pairs produced [48].

This technique possesses a few key advantages. First and foremost, their fast response (μseconds) and reasonable sensitivity make them ideal for dosimetric purposes [1, 49]. Furthermore, they are readily miniaturized thanks to their vital role in modern computer micro-processing and are mechanically stable.

Semiconductor technology for radiation detection still possesses drawbacks. Thus far diode dosimeters have not been used as surgically implanted devices, and their use has been limited to skin, behind-body, and orifices [50]. Additionally, they require electrical wiring, where copper can generate neutrons and other exotic forms of radiation inside the patient's body in the case of proton RT (see Figure 7 [26]). This need for electrical wiring also denotes the detectors reliance on the system operating it. If there is a system failure during irradiation, no more information can be gathered, and no integral dose information is stored in the diode so old data cannot be recovered. This makes diode technology highly fault-susceptible.

Further disadvantages include dependence on dose rate and temperature. The readout of the diode is dependent on the rate of dose entering the diode [51]. Different rates might produce different readouts for the same integral dose. If the diode heats or cools during operation the readout intensity fluctuates accordingly. While temperature sensors and feedback controllers can be used to monitor and control the diode temperature, these all introduce further need for more electronics, greater uncertainty, greater cost, and larger size. Even more, diodes are susceptible to noise and damage from their proximity to the radiation beam and the devices used to produce it. Lastly it has been shown that diode readout is dependent on irradiation angle [51]. As such, diodes are a poor choice for *in-vivo* dosimetry. However, they are excellent devices for monitoring beam current in *real-time* before a patient is to undergo RT.

2.4-h Scintillation Fibers

Scintillator detectors have been in use for decades [1]. Early designs used single-crystal NaI interaction volumes with a set concentration of impurities (usually from some stoichiometric addition of Thallium in the case of NaI crystals, as a dopant). These impurities allow for electron-hole pairs produced by ionization radiation to de-excite through a sequence of radiative emissions in small transitions allowed with the dopant, emitting visible light which can then be counted (refer to Ch. 8 in Knoll for more properties of scintillators, and Ch. 10 for spectroscopy using scintillator detectors [1]). Counting is usually performed using a photomultiplier tube (PMT) with a conversion phosphor screen from photon to electron cascade (refer to Ch. 9 in Knoll for more properties of photomultipliers [1]). The amount of light produced by a scintillator is ideally a linear function of the energy deposited in the interaction volume, though no perfectly linear scintillator exists. Generally, the more light produced in a single radiation detection the more energy was deposited into the interaction volume.

Designs of scintillator detectors for general radiation spectroscopy range from 1" cylinders of 6" length (including PMT and base) to massive multi-foot long spectrometers. These devices are hermetically sealed such that no light or air can enter the interaction volume or the PMT save for the light generated from scintillations in the interaction volume. Additionally, the PMT is almost always directly abutted to the face of the scintillating crystal. These design choices mitigate noise and maximize signal. Despite these efforts even the best scintillation detectors suffer from relatively poor energy resolution, only moderate efficiency due to the hermetical sealing of the device, sizes too large for implantation in medicine, and considerable noise with respect to the signal.

Medical applications require miniaturization in the form of fibrous scintillating material coupled to a PMT using fiber optics. Often these scintillating fibers are made from near-tissue equivalent materials such as polymethylmacrolate giving similar dose response to that of surrounding tissue [52, 53, 54].

Additionally, plastic scintillators have an almost perfectly linear response to dose, with response independent of dose rate. They are also energy and temperature independent [55].

The choice to use plastic fibers was inevitable for miniaturization efforts but gives rise to several additional complications to these dosimeters. First, using fiber optics to couple the PMT to the scintillator greatly reduce the signal amplitude and can become uncoupled entirely, giving a false zero-readout which could result in over-irradiation of a patient. Additionally, the miniature nature of the scintillating fibers means each fiber holds very little material to interact with radiation, reducing efficiency and light yield upon irradiation. Lastly the scintillation fiber contains no integral dose information, so a scintillator detector is only an integral dosimeter if the electronics and optical connections all do not fail. If even one of these portions fails, the dose readout is compromised, and great uncertainty will surround the true dose to an irradiated patient.

2.4-i Prompt Gamma Monitoring

Prompt gammas are a form of radiation emitted when protons impinging on patient tissue excite local atoms to release gamma rays. These gamma rays have distinct energy depending on the species of interaction and their intensity can be used to measure location-specific dose in real time during proton RT [56, 57].

Despite its promise for *real-time* feedback, prompt gamma monitoring has several key drawbacks. Foremost among these drawbacks is the method's reliance on correlations to determine dose. Additionally, recent work suggests that the correlations are, "mostly unknown under real conditions [58]." It is important to note there is continual work to standardize these correlations, but there are only correlations in development for the explicit use of proton RT dosimetry and other forms of RT such as x-ray and gamma are not supported currently with this technique and require further research [59, 60].

Further complications lie with large noise-to-signal ratios in RT scenarios [61]. The equipment used for prompt gamma monitoring is both extremely sensitive and expensive, making its applications limited if not impossible in third-world regions. Lastly, as is a common problem in most dosimetry, if any part of the system fails during operation, integral dose information cannot be gathered. As such this technology is highly *fault-susceptible.*

2.4-j Pet Scans

Pet scans function very similar to prompt gamma monitoring, except in this circumstance it is the 511keV annihilation photons from proton RT-induced positron emission that is used to provide local dose information. Knopf et al. proposed this method as a way to verify the range of the radiation beam used in proton therapy, but with several key exceptions where certain locations in the body proved problematic [62]. Additionally, the location of the annihilation event does not always correlate with position of the initial proton-tissue interaction due to diffusion, notable in soft tissues especially [62]. This technique suffers from the same drawbacks as prompt gamma monitoring, where the equipment required is highly sensitive and expensive, *fault-susceptible,* and large.

2.4-k MOSFET Dosimeters

MOSFET stands for, "metal-oxide semiconductor field-effect transistors." These devices rely on electron-hole pair production from ionizations resulting from irradiation. Holes produced are long lived and migrate to the interface between the silicon substrate and gate oxide where they are sometimes trapped by defects along the interface. This results in accumulation of positive charge at the substrate-oxide interface that in turn changes the how the depletion layer forms when the gate is biased. The threshold voltage required to open the channel between the drain and source contacts is thus altered.

Upon calibration using known sources, one is then able to correlate this change in threshold voltage to the dose received by the oxide layer [63].

This technique is inherently similar to diode dosimetry as it utilizes semiconductors directly interacting with radiation to measure the radiation dose as an electronic signal. However, MOSFETs possess the key advantage that they passively collect radiation information even when the bias voltage is not applied, because the trapped holes are long-lived. They are, additionally, small devices, with cylinder diameters as little as 3mm an 25mm length for the entire dosimetric package [63]. This allows for continued use as an implantable charge counter without need for electronic wiring, as long as the device can be removed from the patient after irradiations and subsequently measured. This makes the device capable of *on-line, fault-tolerant, in-vivo* measurement, but not *real-time* as the device must be removed before being read. *Real-time* applications should theoretically be possible with use of wiring through the patient, but again these electrical connections are undesirable for their interactions with the proton beam.

Chapter 3

Methodology

The following outlines a detailed experiment in which the visible spectral response to proton dose of various alkali halide salts can be measured. Due to numerous delays, this experiment could not be completed by the time this report was formed. The methods outlined can be performed by future users with the experimental setup designed and built as part of completion of this thesis.

3.1 Experimental Setup and Design

To establish criteria for evaluating the efficacy of the IF²D project, it was proposed that various alkali halide salts be irradiated at energies and rates synonymous with proton RT dose, and then their color changes measured. Due to the short timescale of bleaching effects, an experimental chamber was designed to both house crystals for irradiation under vacuum then rapidly switch crystals of interest into an optical assembly capable of measuring color transmitted through the crystal.

3.1-a Salt Wheel

A wheel with 24 slots to house pellet-pressed alkali-halide salts was design such that a simple rotation of the wheel would move a recently irradiated salt directly in the path of the optical system that measures the salt color. The full 3D model of the salt-wheel is given below in Figure 13. The wheel is comprised of 3 parts in addition to the shaft and coupler to the rotary feedthrough. These part's schemata are given below in Figure 14 and Figure 15.

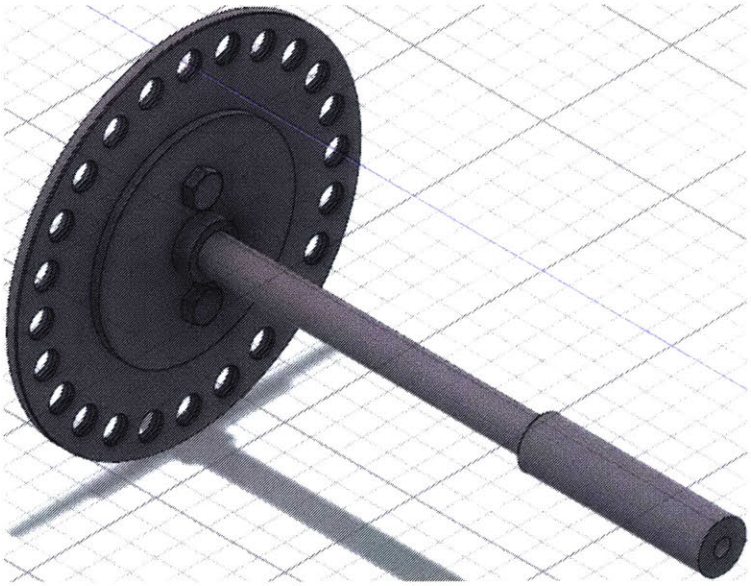

Figure 13: Salt Wheel (fully assembled) – This wheel houses up to 24 pellet-pressed alkali-halide salts which may be irradiated along the proton beam path, then rotated such that they exit the proton beam path and enter the optical assembly to be measured. The wheel is comprised of three parts which fasten together as shown here to hold the salts in place inside of the retainer. Note this does not include the shaft and shaft-to-rotary coupler.

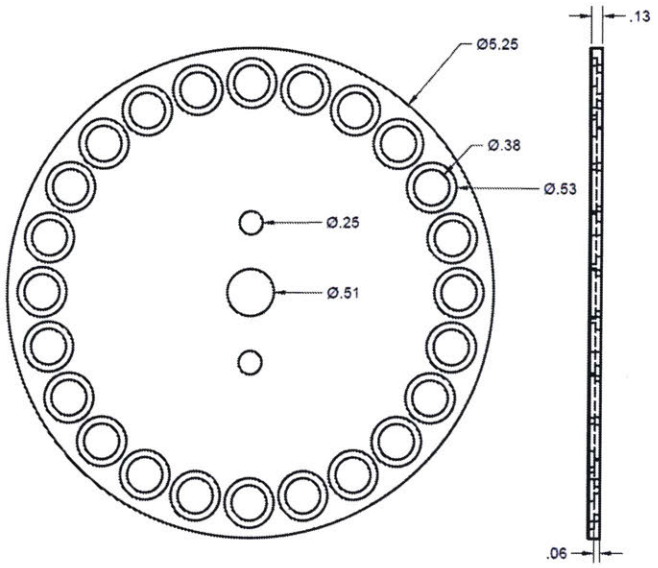

Figure 14: Salt Wheel Holder – This 1/8" thick plate of aluminum was counterbored to 1/16" depth, such that thin pellet-pressed alkali-halide salts could set into the .53" diameter recesses with 0.38" inner bore such that the proton beam and optical path may traverse through the respective salts. This design requires an additional plate as shown below in Figure 15 (A) with 0.38" bores such that the salts do not fall out of the wheel inside of the chamber.

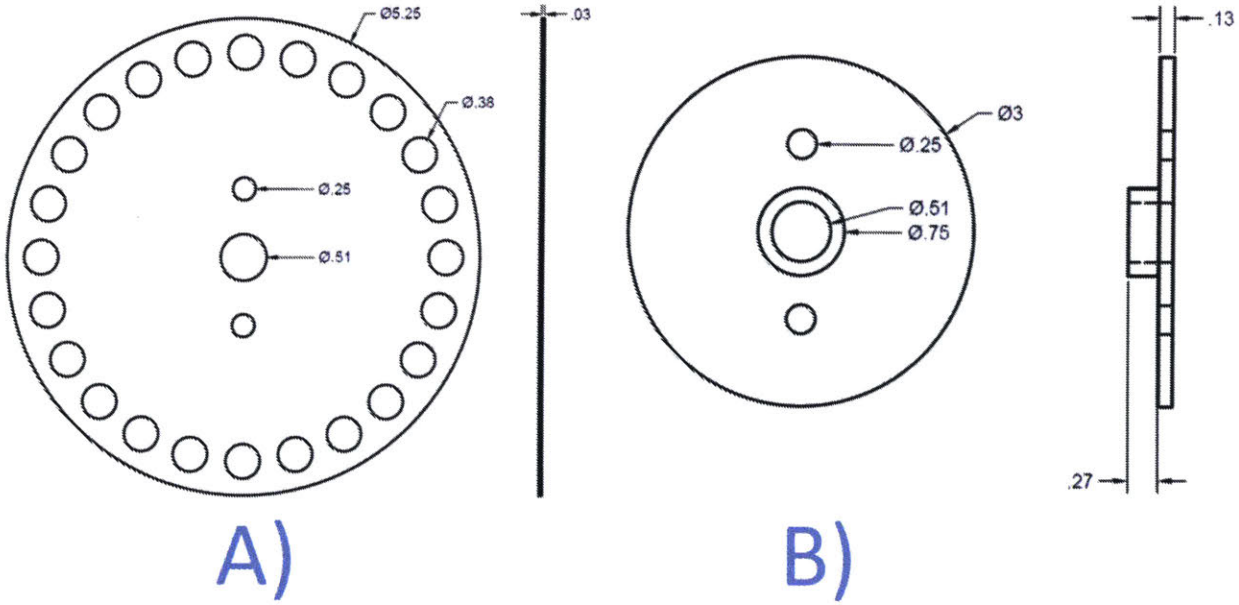

Figure 15: A) Salt-Wheel Retainer – this is a simple stainless-steel plate with 0.38" bores to allow the proton beam and optical path to traverse through the respective crystal without additional material entering these paths. The Retainer is affixed to the holder with the B) Salt-Wheel Fastener – this is a simple aluminum guide to fasten the Holder and Retainer together while simultaneously coupling to the rotating shaft.

All the materials depicted above have already been fully constructed for future use in this project.

3.1-b Optical Assembly

The method for analyzing color change in irradiated crystals relies on the optical assembly, depicted in Figure 16. A broad-band white light is coupled to the collimator on the right of the assembly shown in the figure using fiber optics inside of the vacuum chamber. The collimated light beam traverses from the right to the left until it reaches the first objective lens. Here the collimated beam is focused into the center of the respective alkali-halide crystal set in the optical path using the salt wheel (note the salt wheel is not depicted here but sets between the two objective lenses). The beam fully converges in the crystal center then symmetrically diverges until it reaches the second objective lens, where it is again collimated and focused into a fiber optic coupling system shown on the top left, where 3-axis controls (modified using the knobs) can precisely focus the light back into a fiber optical cable. Both input fiber and output fiber are held inside of the chamber at vacuum, with two optical feedthroughs coupling them to external fiber patch cables that couple to the white light source and photospectrometer respectively.

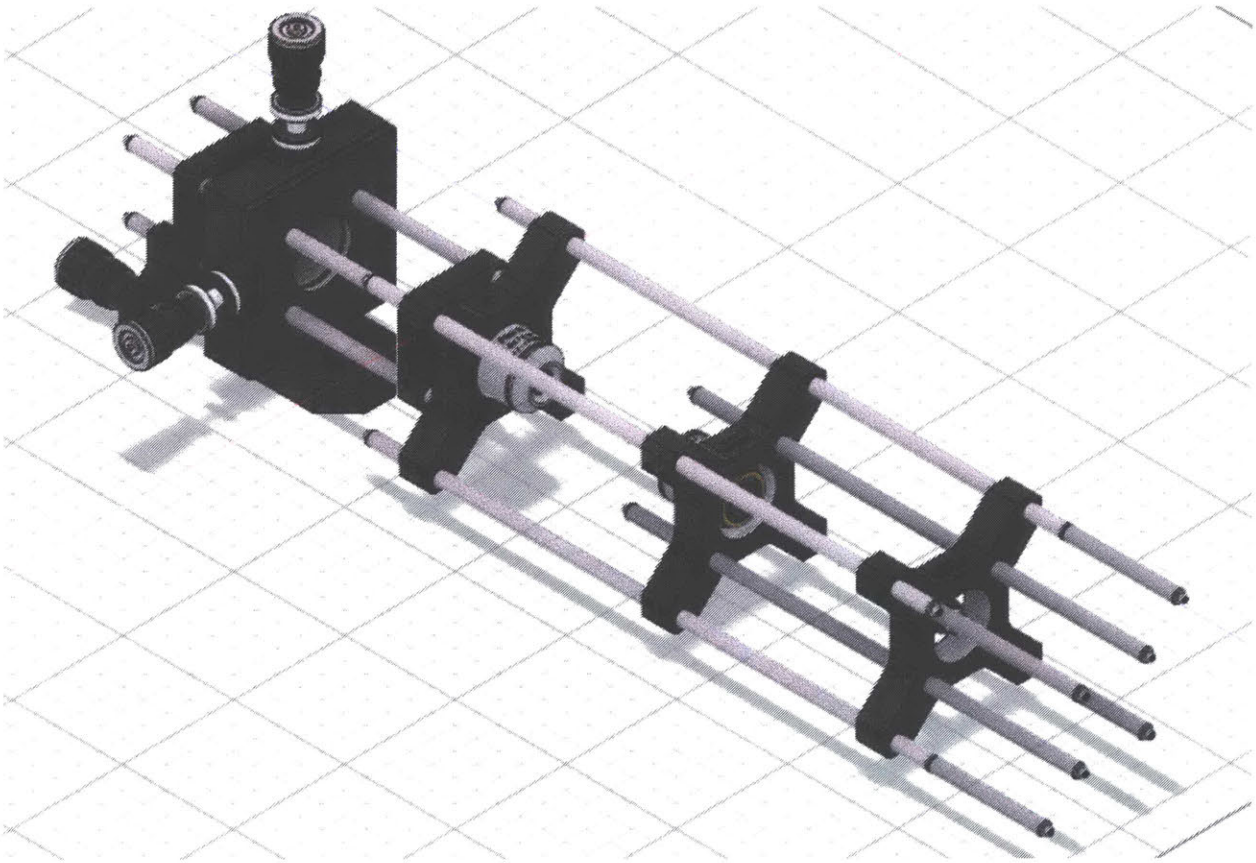

Figure 16: Optical Assembly (fully assembled) – This device collimates a broad-band white light entering from the right through an objective lens that focuses the light into the center of the crystal housed in the salt wheel (salt wheel not shown here). Upon exiting the crystal the light beam is again collimated with a second objective lens that leads to a fiber optic coupler shown on the top left.

The optical assembly depicted above is already fully constructed for future use in this project.

3.1-c Modified 13¼" OD flange

In order to implement the rotary feedthrough and optical feedthroughs the end-cap 13¼" outer diameter (OD) flange was modified at the Central Machine Shop at MIT. The optical components are fed through the larger 2¾" OD inset flange shown in Figure 17. Attached to this flange is a 4-way T-cross with four separate 2¾" OD flanges which attach to the respective two optical feedthroughs and a blank flange to complete the seal. The FRM-133-25 rotary feedthrough attaches to the smaller 1-1/3"

OD flange, allowing for rotation of the salt wheel.

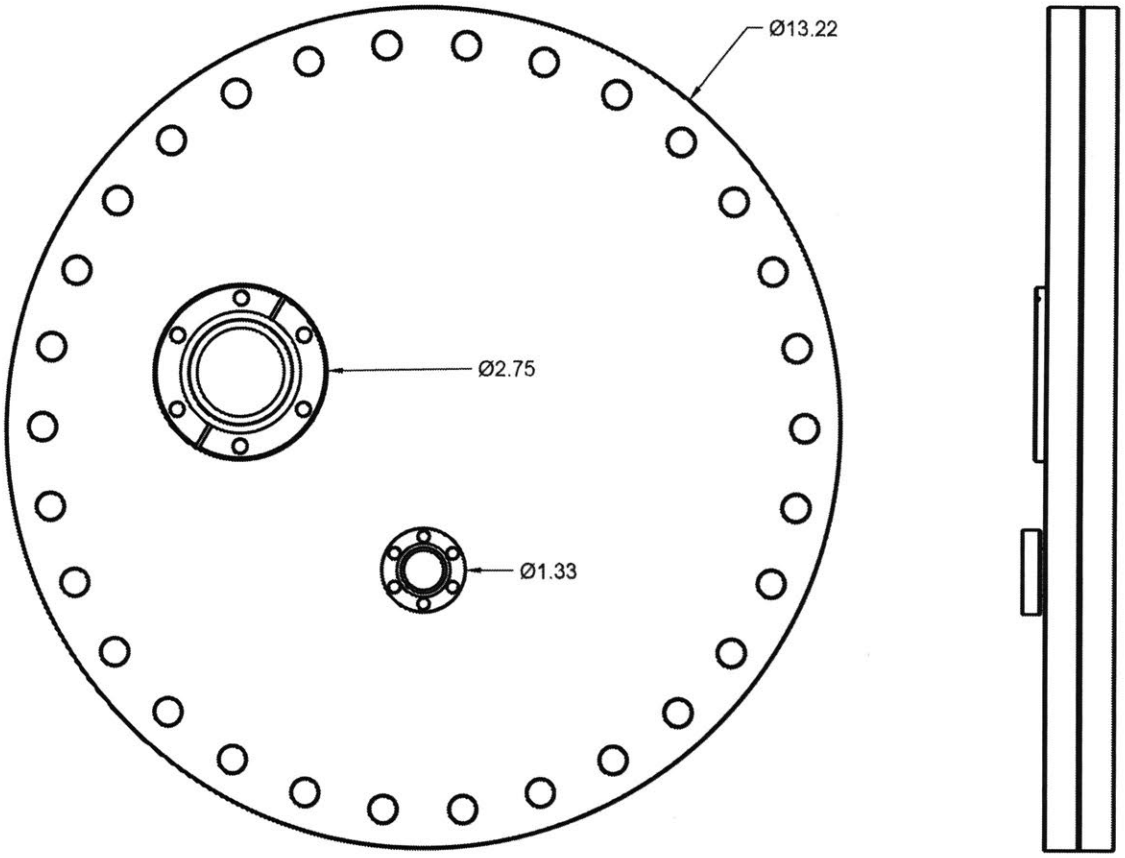

Figure 17: 13.25" OD Flange – this is a modified 13-1/4" OD flange ordered from Kurt J. Lesker. Set in the flange are two flanges, 2-3/4"OD for the optical feedthroughs and 1-1/3" for the rotary feedthrough.

The optical cage is also support on the same 13¼" OD flange. Using 6 of the 7 tapped (4-40) holes seen in Figure 18 (only 6 out of 7 because it was found after assembly that the rotary feedthrough interfered with the cage rod nearest to its position, the bottom left hole) cage rods affixed in these taps support the optical assembly. This design, being only supported from one side, results in considerable torque at the cage-flange interface causing a small amount of sag to occur in which the optical assembly is angled slightly from horizontal due to gravity. This same issue arises with salt wheel. Their cumulative effect has not yet been studied to show with certainty whether additional support is required to allow for proper alignment with the proton beam and with respect to one another.

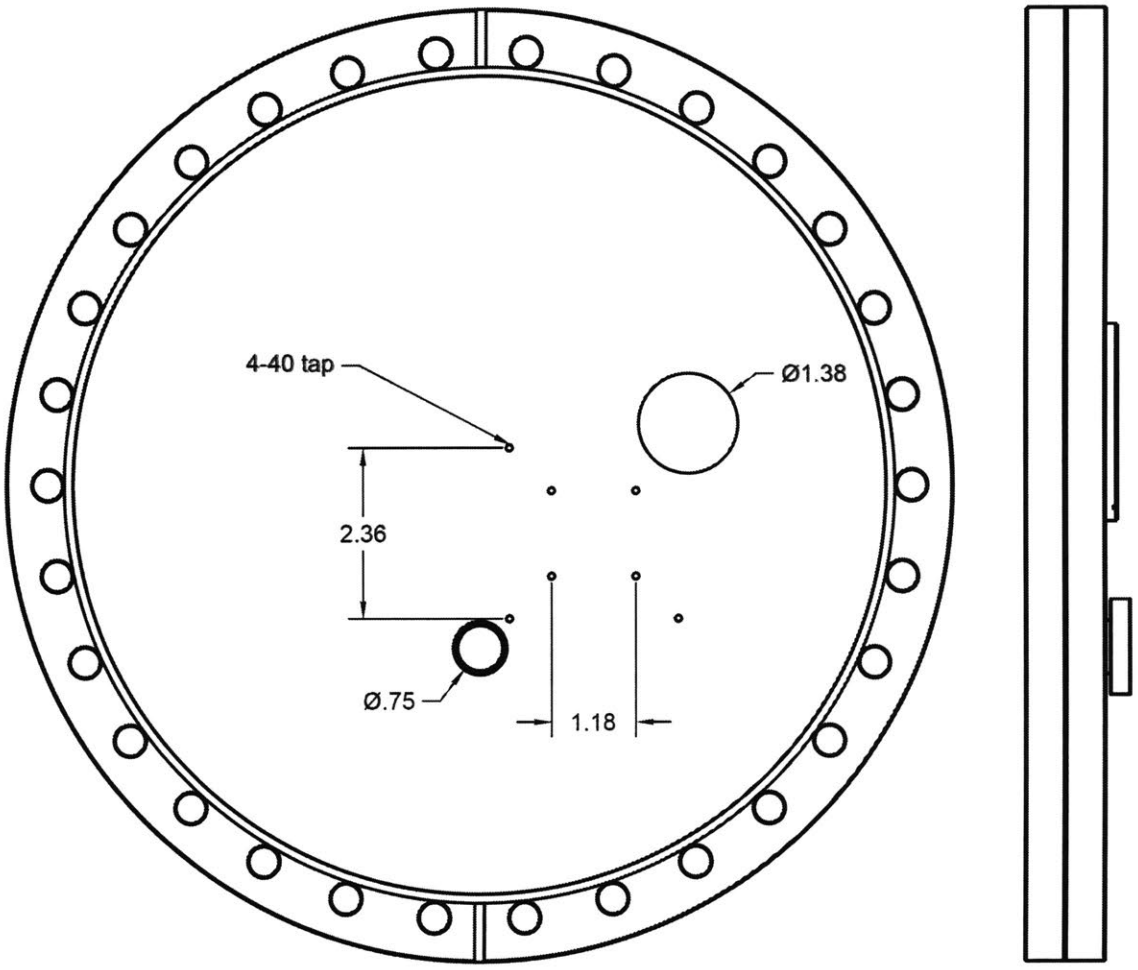

Figure 18: 13.25" OD Flange (vacuum side) – the optical cage is mounted directly into the flange using 6 cage rods ordered from Thorlabs. Additionally the feedthrough diameters are shown. The optical cable feedthrough diameter is of 1.38" to accommodate flexibility of the cables. The rotary feedthrough is of ¾" diameter as is the internal diameter of a 1-1/3" flange and was chosen accordingly.

The 13¼" OD flange depicted above is already fully constructed for future use in this project.

3.1-d Full Assembly

The fully assembled chamber interior with salt wheel and optical assembly included is given in Figure 19. In this figure, the proton beam enters the chamber from the right side. The assembly is attached to the accelerator with precision such that the proton beam is perfectly centered with respect to the 13¼" outer diameter (OD) flange (left side, more details shown in both Figure 17 and Figure 18), 13¼"-to-8" adapter (right side), and nipple (nipple not shown here, refer to Figure 20). The optical cage is positioned such that no part of the assembly enters the proton beam path. The salt wheel is positioned such that the top hole is centered with respect to the beamline, while still able to rotate into the path of the optics for measurement.

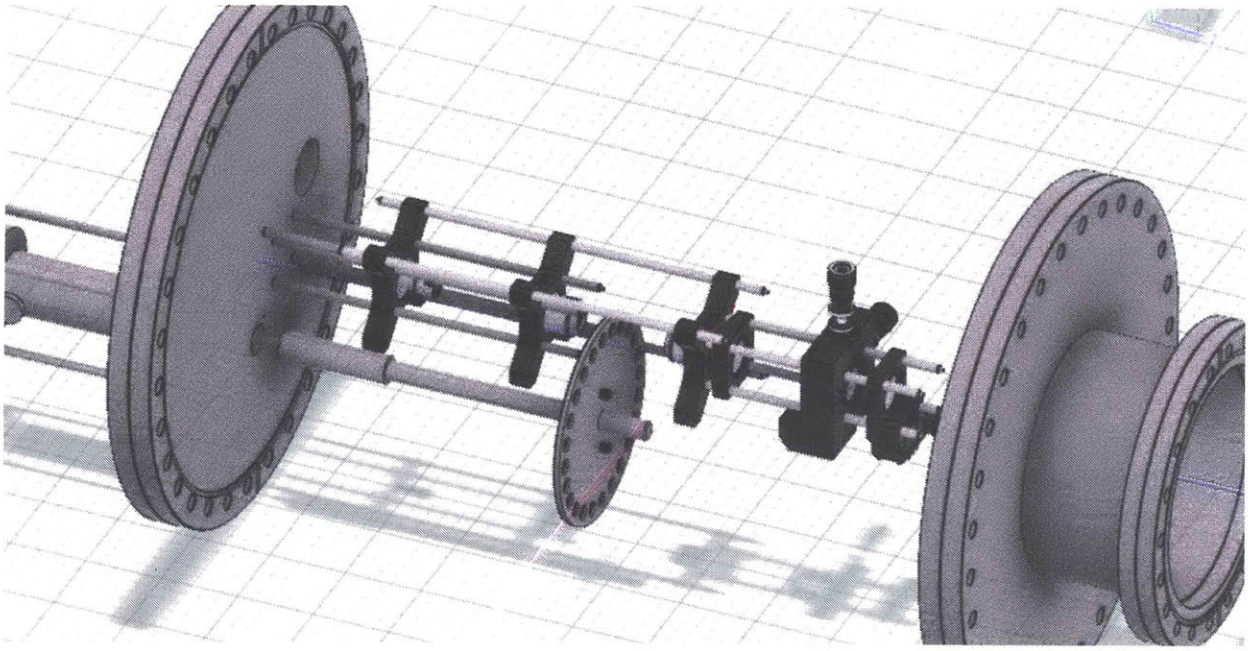

Figure 19: Full Assembly Interior – the configuration of salt wheel to optical assembly inside the vacuum chamber is shown. Note the vacuum chamber and its supports are not shown here, refer to Figure 20 for the exterior picture. The proton beam enters the chamber from the right travelling leftward, perfectly centered with respect to the flange and 13.25"-to-8" adapter. Once irradiation of the species of interest is completed the beam is cut off and the salt wheel is rotated such that the recently-irradiated salt is moved from the proton beam path into the center of the optical path. By measuring the change in transmitted spectra, the F-center production can be quantified and potentially be of use for designing a full dosimeter.

The exterior of the full assembly is show in Figure 20 (note this is a 180° rotation with respect to Figure 19). The proton beam enters perfectly centered from the left and interacts with the respective salt crystal on the inside. The vacuum chamber seen is a 20" nipple of 13¼" outer diameter (OD) flange couplings on both ends. Affixed to the left side of the chamber depicted in Figure 20 is the 13¼"-to-8" converter to attach the large chamber to the beam port. Affixed to the right side of the chamber is the modified 13¼" flange depicted in both Figure 17 and Figure 18.

The optical feedthroughs are not depicted here, but the rotary feedthrough is shown attached to the 13¼" flange, with its respective knob affixed using 4 cage rods. The rotator model is the Thermionics Northwest FRM-133-25 rotary feedthrough. This feedthrough allows the salt wheel on the interior (vacuum side) of the chamber to be rotated from the outside of the assembly. This gives the operator easy control of the wheel without needing to vent the chamber to make rotational adjustments. This rotary is attached to a custom-built knob with 24 knocks to hold the wheel in the exact position required to irradiate and measure color.

Owing to the device's large size, considerable structural support is required to hold the chamber in place once installed. This is done using rotatable angle brackets, t-slotted framing, and screw-in feet as seen on the bottom of the chamber picture in Figure 20. The six legs are affixed to a larger structure with 4 horizontal strips of T-slotted framing at its top (the larger structure is not depicted here, except for the top 4 strips of framing). Together these legs support the 100+lbs of the full assembly.

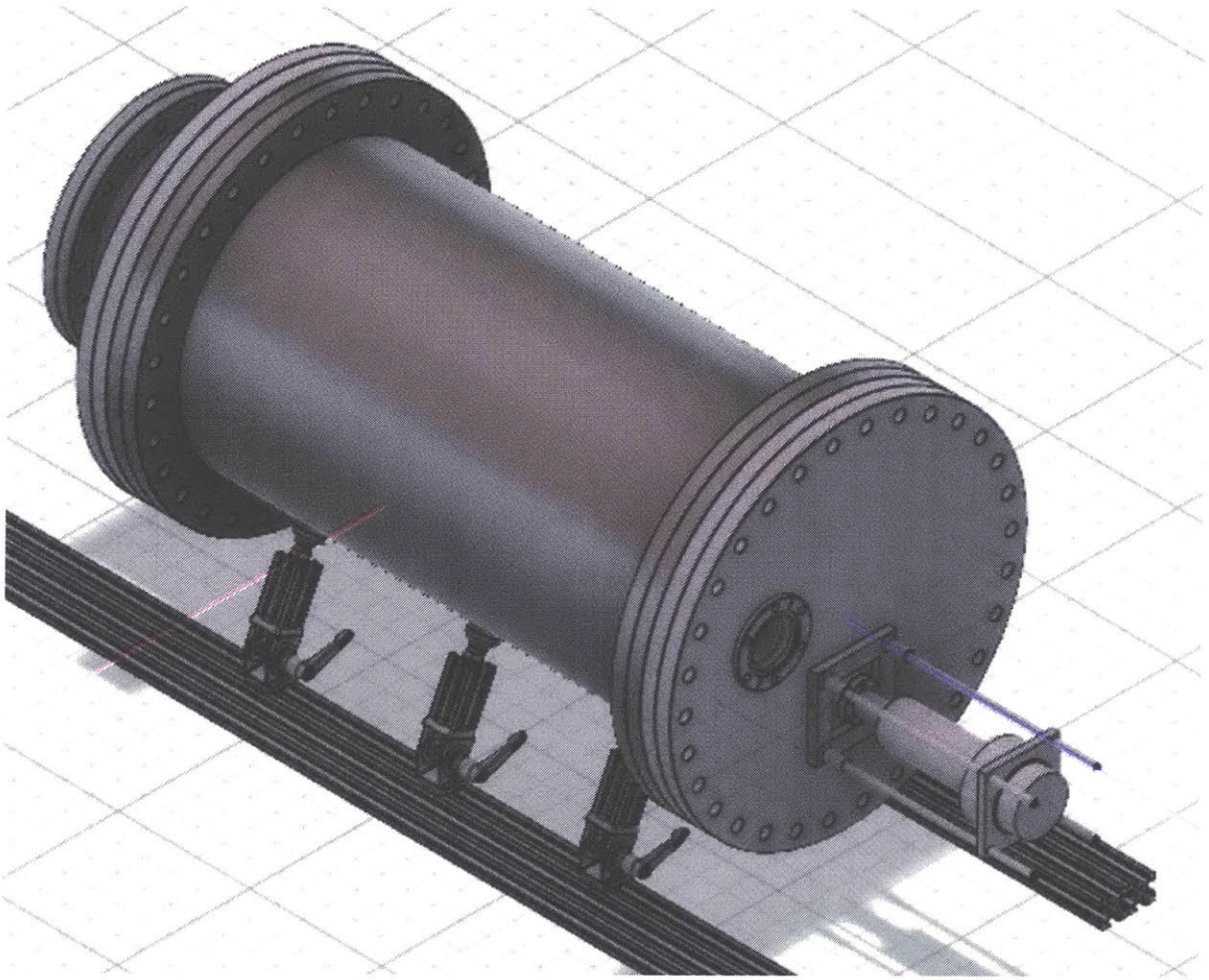

Figure 20: Full Assembly Exterior – This shows the exterior of the experimental chamber seen from the perspective of those performing the experiment. The vacuum chamber is comprised of a 20" nipple with 13.25" OD flange couplers which fasten to the 13.25" OD flange shown on the right and the 13.25"-to-8" flange adapter shown on the left end. The chamber is supported by six legs affixed to McMaster T-Slotted Framing for structural support during irradiation. On the right face is the rotary feedthrough and 24-slot knob allowing for rotation of the salt wheel from the exterior by simple use of the knob.

All components of the full assembly depicted above are already fully constructed for future use in this project. The chamber was fully assembled and attached to the beamline save for coupling the 13¼" OD flange to the vacuum chamber. Upon loss of a vital component during this process irradiations could not be performed in time for this report. However, upon replacement of a single fiber optic patch cable, the assembly will be full ready for experimentation so as long as the sagging issues with the optical cage and salt wheel are not too severe to warrant further construction.

3.2 Experimental Procedure for Full Assembly

The purpose of this experiment is to determine how the spectra gathered from white light transiting through various alkali halide salts changes upon irradiation. As such a broad-band LED with approximately white color (note: the visible color of this beam is much closer to that of yellow) is operated externally from the chamber for a number of minutes until the heating from the LED stabilizes with the cooling rate in its environment. At this time a full measurement may be performed.

Measurements are taken as follows:

1. The broad-band white-light is left on for at least one minute such that it's temperature of operation approximately stabilizes
2. A pure transmission spectrum is gathered using a CCS100 photospectrometer purchased through Thorlabs. This spectrum is referred to as a transmission spectrum as no material – salt or otherwise – is in the optical path. This is performed through a slot left empty in the salt wheel.
3. An unirradiated salt is rotated into the path of the optical system
4. The salt is illuminated in the optical path and the resulting photospectrum is gathered, serving as baseline with respect to the irradiated spectrum.
5. The same salt is immediately rotated into the center position of the proton beam
6. The respective salt is irradiated by activation of the proton beam
7. Once the full dose is given, irradiation is halted by deactivation of the proton beam
8. The wheel is rotated such that the same salt is back in the optical path.
9. The irradiated salt is illuminated in the optical path and the resulting photospectrum is gathered.

The two baseline measurements serve as control to measure minute-by-minute color changes that occur when the broad-band white-light LED heats and cools in its environment. The LED becomes noticeably warm to the touch within a minute of operation, despite the heat sink. As such it is vital the resulting spectral fluctuations are noted with absolute precision to mitigate noise and false spectral changes that are not the result of crystal color change.

3.3 Pellet Pressed Alkali-Halides vs. Single Crystal Salts

Both single crystal salts and multi-crystal pellet-pressed salts are under investigation in this experiment. Single crystal salts were purchased with 99.9% seller-rated purity, though the purity estimate was not verified experimentally, namely NaCl, KCl, and KBr. In addition to these single crystal salts, powdered salts were purchased including:

- KCl
- KBr
- KI
- NaCl
- NaBr
- NaI
- LiF

These salts were chosen arbitrarily based on availability and/or mention in literature. All salts purchased, with exception of LiF, have F-center bands in the visible spectrum. LiF was purchased with the possibility of a new experiment in which both the radioluminescence and thermoluminescence of the crystal would be measured in conjunction to explore its various properties for dosimetry. This was informed by its current use in TLDs (refer to section 2.4-a). However, due to project delays such an experiment was never designed and no material to share is presentable in its current hypothetical state.

The salts listed above (again excluding LiF from here and on) were purchased in powder form, heated in vacuum oven for 24hr, ground to a fine powder with near-paste consistency, and then reheated for another 24hr. After this treatment the powders were sifted to 63μm or finer and then immediately pressed. The pressing procedure involves the use of a PIKE brand 13mm pellet die, depicted in Figure 21.

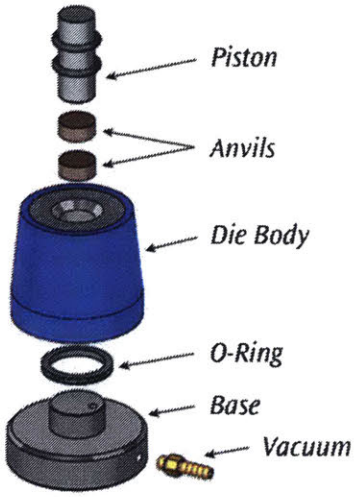

Figure 21: A PIKE-brand 13mm evacuable die was used to prepare salt pellets for irradiation. Small amounts of powder salt ranging from approximately 100mg to 250mg were placed between the two anvils shown. After vacuum was drawn, 18,000lbs of force was applied (through methods outlined below) between the two anvils via the piston, supplied by a 9-ton pellet press, forming a transparent salt pellet for use in the salt wheel.

The pellet pressing procedure used is as follows:

1. The die body, O-ring, and base are assembled
2. Finely ground and sifted, desiccated, salt-powder is loaded into the pellet die between the two pistons
3. The piston is installed
4. Vacuum is drawn in the die for 30 seconds via hose and vacuum pump
5. 5 tons of force is applied using the press and then is released to 0 tons immediately
6. Die is evacuated for another 30 seconds
7. 7 tons of force is applied using the press and is held at this pressure for 30 seconds then released to 0 tons
8. Die is evacuated for 1 minute
9. 9 tons of force is applied using the press and is held at this pressure for 2 to 3 minutes the released to 0 tons
10. Die is removed from press and salt pellet is delicately extracted from the die

This technique was developed over the period of several months as earlier dies and attempts without a sieve produced opaque or nearly-opaque pellets. It was found that without use of the sieve, the pellets contained numerous opaque spots with transparent surroundings, suggesting larger grains in the sample created nucleation cites in which defects clustered and formed regions far more opaque than surrounding material. Even then, the transparent regions were of high opacity relative to a perfectly clear crystal. Upon purchase the PIKE die, which holds vacuum far better than prior dies, the pellet quality increased dramatically. While the same pressure was applied to the PIKE die as to prior dies, the ability

to hold vacuum removed air that contained moisture. Given alkali-halide salts' propensity to absorb moisture from the air and turn opaque, this was not surprising.

Numerous salts were produced for the experiment and are on standby for future use in the vacuum chamber. However, due to numerous project delays, experimentation on pellet-pressed salts has yet to be performed.

3.4 Experimental Procedure for Single Crystal Irradiation

A preliminary round of irradiations was performed prior to full development of the salt-pellet irradiation system. Three irradiations on 1cm cubic single-crystal salts were performed in a separate vacuum chamber housed as default along the accelerator beamline. First a single transmission spectrum was taken as baseline, then 3 separate spectra for transmission through each unirradiated crystal.

All crystals were irradiated one at a time, housed in the same chamber as the others, with a 100kGy target-dose. Once the last crystal was irradiated the salts were removed from the chamber and their spectra were recorded, noting the time for each between end of irradiation and measurement with about ± 30 seconds of type-B uncertainty (arbitrary estimate) due to a stopwatch failure between the time in which the crystals were removed from the chamber and their spectra were recorded. This uncertainty estimate was obtained by counting aloud the time between noting the stopwatch failure and resetting the stopwatch.

Irradiations were performed using the CLASS Tandem Accelerator at MIT. To toggle the beam, a faraday cup was placed in or out of the beam path to turn it off or on respectively. This cup was inserted manually via linear-feedthrough. Samples were first aligned with the beam while the faraday cup was inserted ensuring no current was yet to reach the respective crystal. One operator managed the faraday cup while the other manned the stopwatch and called out when to insert or remove the cup, noting the time at which the call was made as read on the stopwatch, allowing for the times of each event to be recorded. It is vital to note this method gives rise to considerable type-B uncertainty as the reaction times of not just one, but two operators were involved to irradiate the target. It is estimated that this could leave up to as much as a 3 second discrepancy between recorded and actual time.

Chapter 4

Results and Discussion

4.1 Projected Results from Literature

Prior to experimentation, literature was first consulted to predict the F-band locations for various salts, as well as project what effect dose has on the F-band absorbance. below in Table 1 is the number of sources for each type of salt. The sources themselves are given in Table 2.

Table 1: Source breakdown by number for the derived plots shown from Figure 22 to Figure 24. Note this includes overlap of sources.

Salt	Sources
KCl	4
KBr	2
LiF	4

Table 2: Sources whose data is directly used for the derived plots from Figure 22 to Figure 24. Some salts use the same source as another.

Salt	Reference (citations also included in reference section at the end of this document)
KCl	K. V. Rao, "Colour Centre PHenomena in Alkali Halide Crystals X-Ray-Irradiated Under High Electric Fields," *Nuclear Tracks and Radiation Measurments*, vol. 10, no. 1-2, pp. 203-214, 1985. [64]
	D. Pooley, "The Saturation of F-Centre Production in Alkali Halides Under Proton Irradiation," *British Journal of Applied Physics*, vol. 17, pp. 855-861, 1966. [65]
	A. E. Hughes and D. Pooley, "High Dose Proton Irradiation of Alkali Halides," *J. Phys. C: Solid St. Phys.*, vol. 4, pp. 1963-1976, 1971. [66]
	H. N. Hersh, "Studies of Color Centers in Polycrystalline Compressed Pellets of Alkali Halides*," *The Journal of Chemical Physics*, vol. 27, no. 6, pp. 1330-1338, 1957. [67]
KBr	J. Markham, R. Platt and I. Mador, "Bleaching Properties of F Centers in KBr at 5K," *Phys. Rev.*, vol. 92, no. 3, pp. 597-603, 1953. [9]
	H. N. Hersh, "Studies of Color Centers in Polycrystalline Compressed Pellets of Alkali Halides*," *The Journal of Chemical Physics*, vol. 27, no. 6, pp. 1330-1338, 1957. [67]
LiF	M. Piccinini, F. Ambrosini, A. Ampollini, M. Carpanses, L. Picardi, C. Ronsivalle, F. Bonfili, S. Libera, M. A. Vincenti and R. M. Montereali, "Optica Spectroscopy and Imaging of Colour Centres in Lithium Fluoride Crystals and Thin Films irradiated by 3MeV Proton Beams," *Nuclear Instruments and Methods in Physics Research B*, vol. 326, pp. 72-75, 2014. [68]
	W. L. McLaughlin, A. Miller, S. C. Ellis and A. C. Lucas, "Radiation-Induced Color Centers in LiF for Dosimetry at High Absorbed Dose Rates," *Nuclear Instruments and Methods*, vol. 175, pp. 17-18, 1980. [10]
	W. L. McLaughlin, A. C. Luca, B. M. Kapsar and A. Miller, "Electron and Gamma-Ray Dosimetry Using Radiation-Induced Color Centers in LiF," *Radiat. Phys. Chem.*, vol. 14, pp. 468-480, 1979. [69]
	F. Morehead and F. Daniels, "Thermoluminescence and Coloration of Lithium Flouride Produced by Alpha Particles, Electrons, Gamma Rays, and Neutrons," *The Journal of Chemial Physics*, vol. 27, 1957. [11]

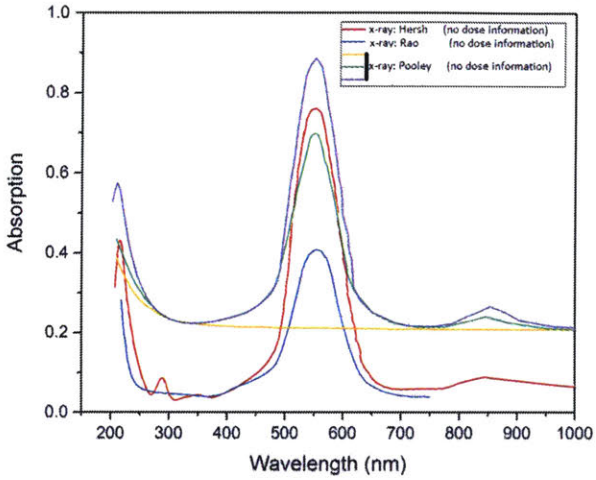

Figure 22: KCl– The spectral dimming band for KCl appears between 500nm and 600nm. For X-rayed doses, Pooley's [65] work did not specify the dose to the crystals in Gy, only noting the beam was of 300keV photons for their respective times with a current of 0.38μA, without giving the crystal masses required to calculate integral dose. Similar problems face Hersh [67] and Rao's [64] work, and no integral dose information could be gathered. However, this illustrates the approximate location of the F band, and is useful for reference for analysis.

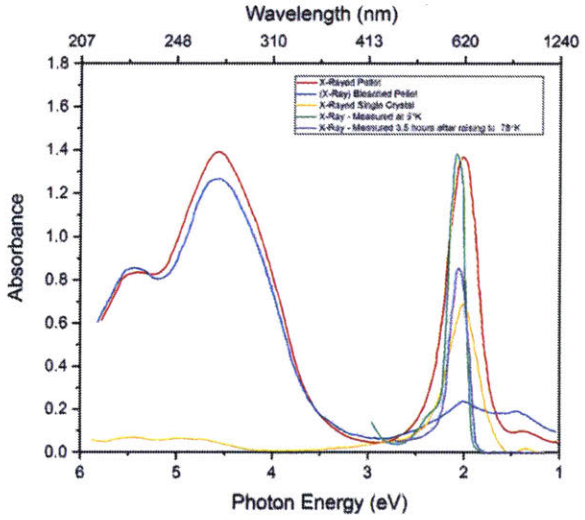

Figure 23: KBr – Cumulative dose information for all curves here could not be found. However, this figure is still useful in that it illustrates the location of the F-band at approximately 620nm.

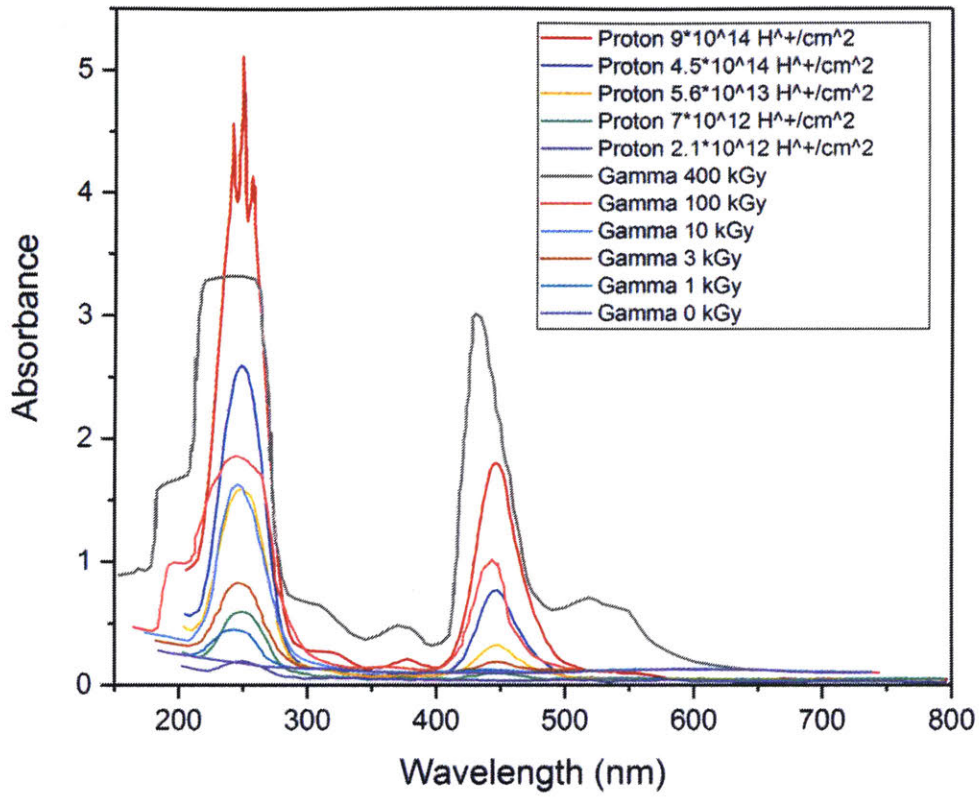

Figure 24: LiF – The F-band for LiF is in the ultraviolet region, and thus is not of principle interest for this project. However, the existence of an additional color band at 450nm, reportedly the result of the M-band [68], allows for potential use in dosimetry provided the LiF is not irradiated with protons, as protons impinging on lithium may produce neutrons and other subsequent forms of harmful radiation.

The data presented in Figure 22 through Figure 24 show in good agreement among literature the proximal locations of the F-center color-absorbing bands. Many figures derived therein were given inadequate dose information or none whatsoever. As such it's not possible with this data to predict the spectral band intensities likely to be seen when data is taken in accordance with the procedure outlined in section 3.2. However the locations of the spectral bands can be predicted using the data presented.

4.2 Single Crystal Irradiation results

The experimental procedure outlined in section 3.2 was not performed due to various unforeseen project delays. However, a single preliminary experiment was performed as outlined in section 3.4. The transmission spectrum was initially fully saturated, meaning the data appeared as a horizontal line at 100%, making no meaningful observation possible. The alignment of the fiber coupler (the 3-axis coupling system pictured on the top left of Figure 16 in section 3.1-b) was adjusted until the light was dim enough to be read. After this adjustment the optical assembly was not moved or recalibrated until after the experiment was over. Below is the transmission spectrum, namely the spectrum in which no salt is being measured, in Figure 25.

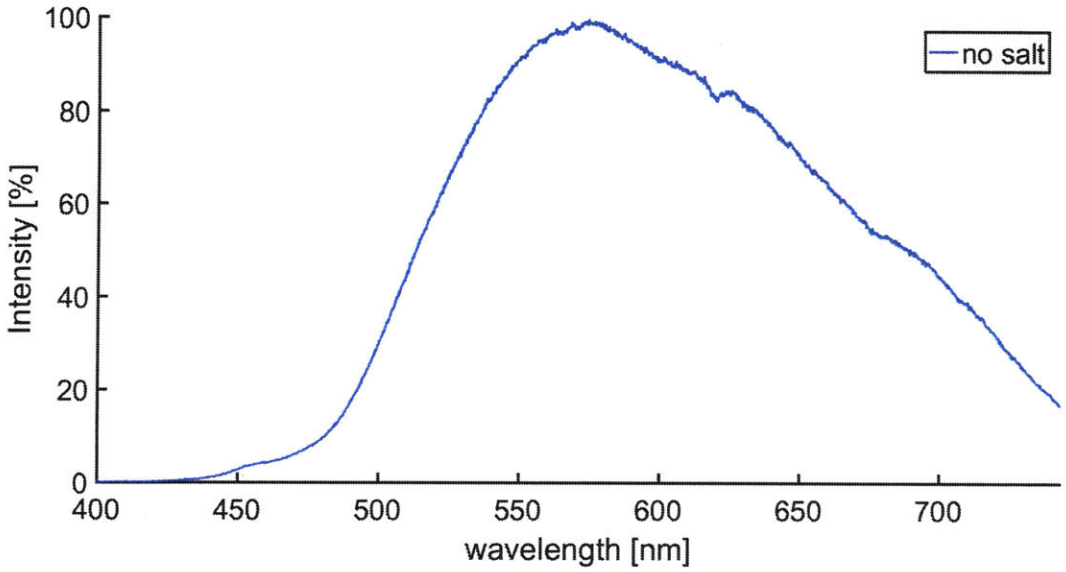

Figure 25: Transmission Spectrum – This is the photospectrometer reading produced when shone directly with the broad-band white-light LED, with no salt or other material in the optical path.

Note that in Figure 25 the spectrum is plagued with noise, as are all base-spectra for this experiment. There was a user error when saving these spectra, where 1000 sample average was intended to be saved but instead only a single sample was captured. As one will see, this compromises the integrity of this experiment almost entirely. Below, in Figure 26, are the baseline spectra for each salt with respect to the transmission spectrum.

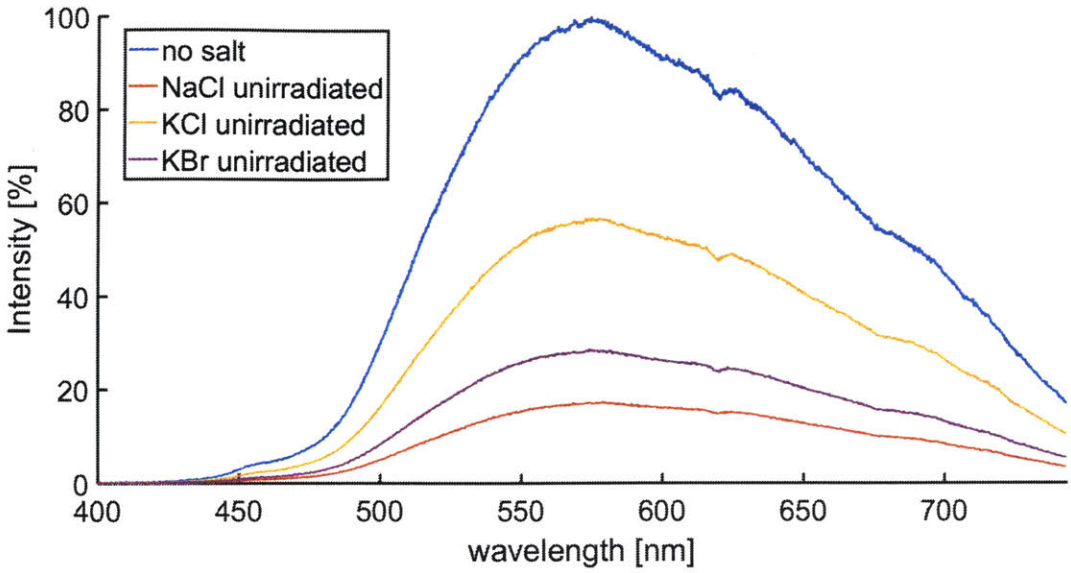

Figure 26: Baseline Spectra – Each of the three single-crystal salts were measured in the optical assembly prior to irradiation for control. Each salt, while single crystal, was plagued with surface defects that increased their opacity.

As seen in Figure 26, small surface defects in the single crystals resulted in a surface opacity that limited the signal strength through the crystals. Generally, the pellet pressed salts give better transmission strength for unirradiated crystals, owing to their transparency.

Each salt, NaCl, KCl, and KBr, was then irradiated with 2MeV protons in a chamber that was already part of the accelerator. *Bragg Curves* were generated by the accelerator operator which showed the implantation depths (center of *Bragg Peak*) ranging between 42.1μm to 55.2μm into the crystals. When accounting for the beam current, the dose rate was estimated for each crystal as follows:

- NaCl: 247kGy/min (depth ≈ 52.3 μm)
- KCl: 237kGy/min (depth ≈ 42.1 μm)
- KBr: 166kGy/min (depth ≈ 55.2 μm)

As outlined in section 3.4, the times for starting and stopping the proton beam are uncertain up to 3 seconds, estimated arbitrarily as type-B uncertainty. The subsequent doses to each crystal, with their respective times and uncertainty, are given below:

Table 3: Irradiation Results – Each salt was irradiated with a 100kGy target dose. However due to user error and uncertainty no salt was irradiated to precisely 100kGy, but rather ranging from 75kGy to 90kGy with uncertainties between approximately 10%-13%.

Salt	Target time for 100kGy [sec]	Real time (type-B uncertainty) [sec]	Estimated dose (type-B uncertainty) [kGy]
NaCl	22.1 sec	22 ± 3	90 ± 12
KCl	23.0 sec	24 ± 3	95 ± 12
KBr	32.9 sec	27 ± 3	75 ± 8

The times between the end of the irradiations and the subsequent spectral measurement of the respective salt are given below:

- NaCl: 566 ± 33 seconds
- KCl: 610 ± 33 seconds
- KBr: 461 ± 33 seconds

The resulting spectral changes are given below in Figure 27, Figure 29, and Figure 28.

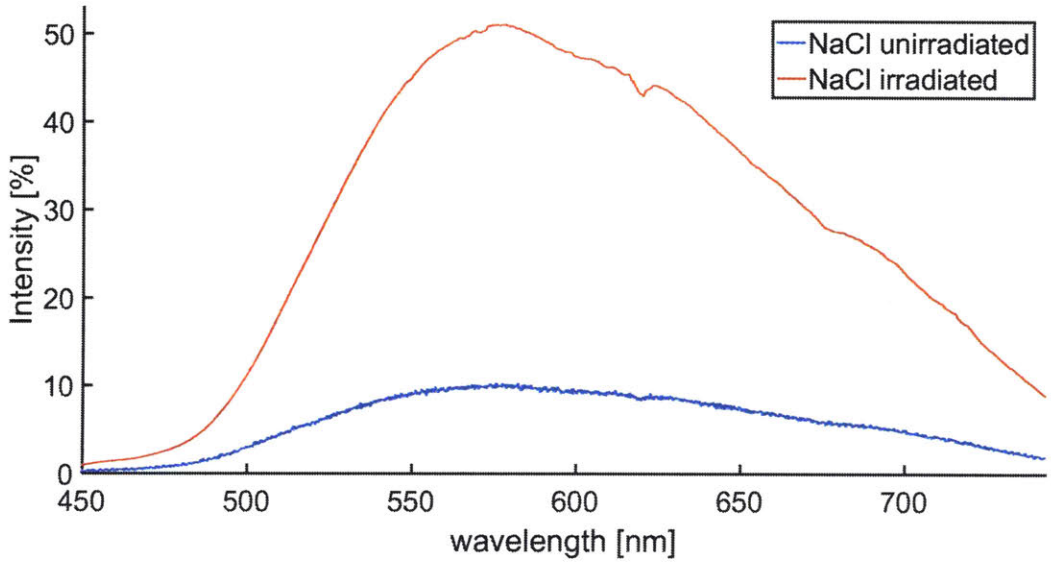

Figure 27: NaCl Spectral Shift – Data for this plot is particularly dubious, as it appears there was considerable error in taking baseline measurements for NaCl. The baseline should never appear below the irradiated spectrum, as irradiation only induces opacity and color change effects. As such this data is not usable.

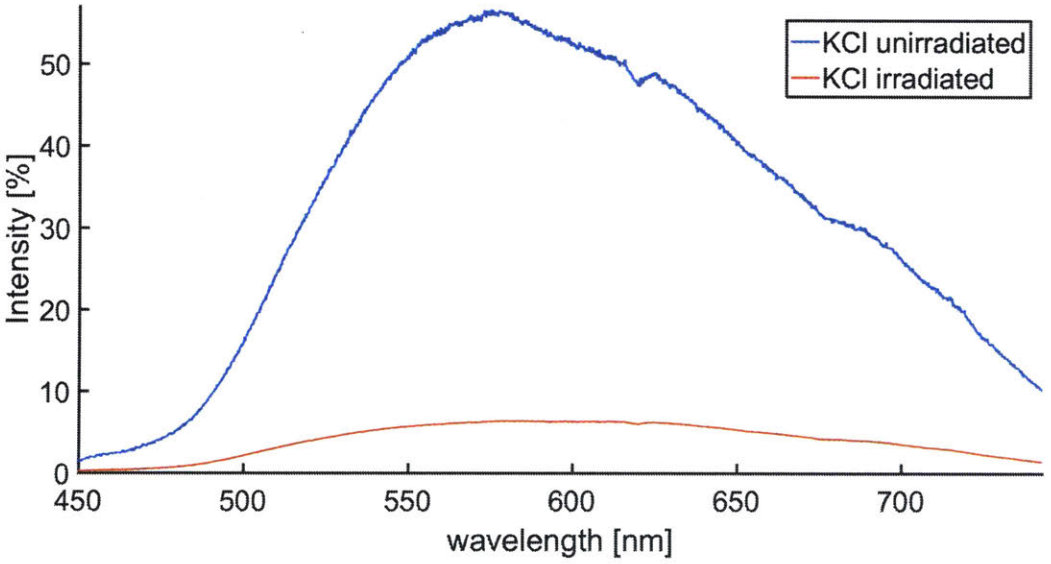

Figure 28: KCl Spectral Shift - The considerable broad-spectrum dimming of the crystal appears to be the result of changing crystal alignment between baseline and irradiated readings rather than actual spectral change. Because only a single pulse was integrated for the baseline, there is too much noise to distinguish any noticeable band-dip features in the crystal.

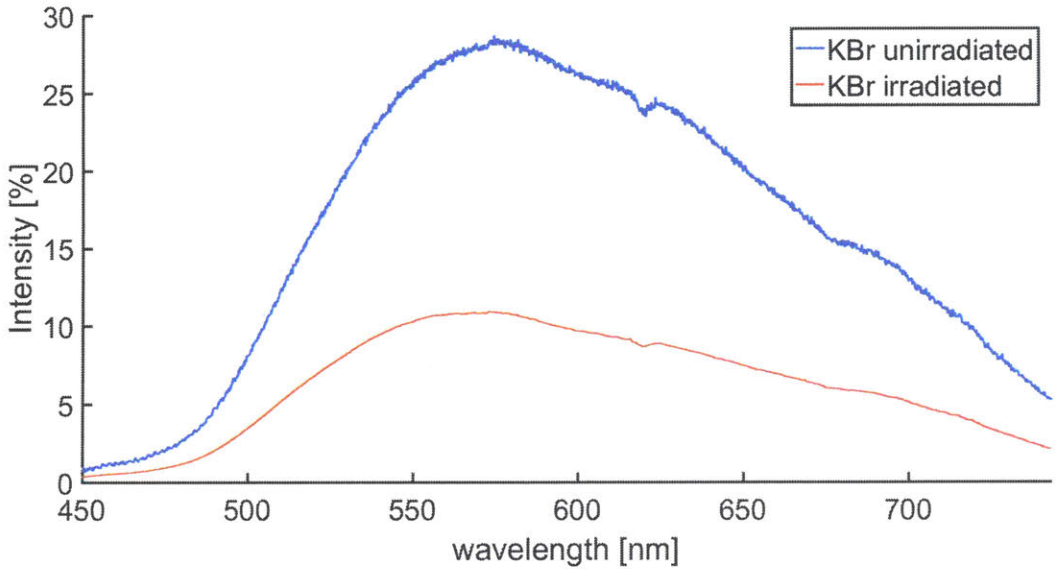

Figure 29: KBr Spectra Shift – Again a similar pattern is noted as found with KCl, that the broad-spectrum dimming of the crystal very well may be the result of changing alignment with the crystal position in the optical path rather than any true spectral bands forming. Additionally, the noise in the baseline makes for inadequate comparison of these two spectra, and thus no definite spectral can be found.

As seen the data are not remotely comparable due to massive signal drift from the time of measuring the unirradiated and irradiated spectra. This is the result of inconsistent alignment of the crystal in the optical path between these measurements, as well as the operator error in taking only a single pulse for the unirradiated spectra vs the 1000 pulses taken for the irradiated spectra. More valuable is an image taken of the salts approximately 10 minutes after irradiation shown below in Figure 30.

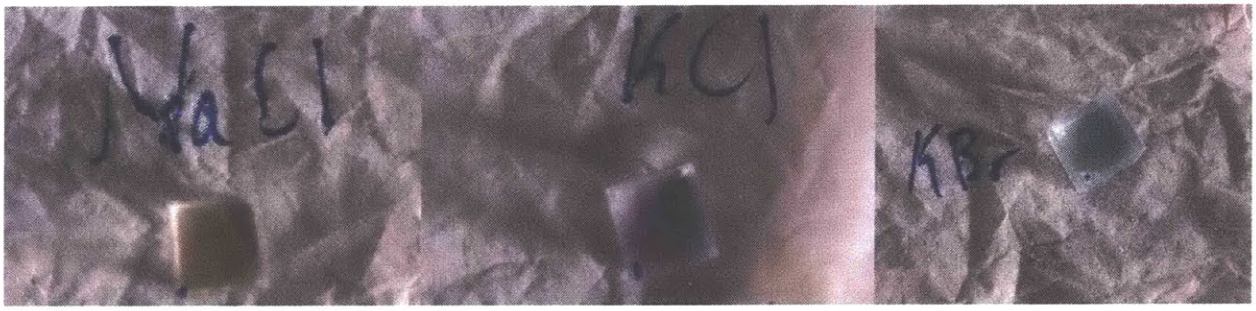

Figure 30: Doses approximately at 100kGy were delivered to each crystal with implantation depths near or around 50μm. This picture was taken approximately 10 minutes after irradiation had ended for the crystals, showing that the crystals changed color visibly. NaCl turned proximally yellow, while KCl purple, and KBr light blue.

As seen in Figure 30, the salts did change color noticeably by cursory inspection. NaCl formed yellow discoloration while KCl was purple. KBr, likely due to the large dose deviation from 100kGy unlike the other two salts, showed only a faint color shift towards light blue.

As seen for KCl in Figure 22, the F-band *absorbs* light in the 500-600nm region, or green to orange. This means the red and blue color regions are the dominant colorations for the crystal, forming purple. Comparing this with Figure 30, it appears results of coloration are in good agreement with literature.

For KBr, highly absorbing spectral bands appear around 280nm and 620nm. Light with wavelength of 280nm is not visible to the human eye so no coloration should be produced from this band. However, 620nm is firmly in the red color region, indicating irradiated KBr should *absorb* red, resulting in a mostly blue coloration of the crystal. By inspection of Figure 30 this appears again in good agreement with literature.

In addition to measuring color immediately after irradiation the salts were imaged the next day (≈20hr) and found to have no coloration both visible or measured by the photospectrometer. It is assumed that the bleaching rates are on the scale of hours and thus meaningful data collection must occur within minutes of irradiation.

This data demonstrates that both the salts indeed change color upon irradiation (though the color change is faint for even high doses) and that the bleaching rates are too rapid for passive integration over the period of several hours. However, the salts are passively integrating (when accounting for spontaneous bleaching) in the dark for timescales on the order of several minutes. This still allows for potentially real time feedback *during* irradiation and with the possibility of recovering some dose information shortly thereafter.

Chapter 5

Conclusions

Work performed shows that the alkali-halide salts bombarded do change color upon irradiation, though the color change is faint even for high doses. Additionally, it was found that the bleaching rates in NaCl, KCl, and KBr are too rapid for passive integration over the period of a few hours or more. These results, while not ideal, do not fully invalidate the IF^{2}D project's underpinnings and future work may find more adequate methods to refine measurements in and around proton RT doses. Future work to be performed for this experiment includes characterizing the bleaching rates of pellet-pressed alkali halides, which may retain F-centers over longer periods, such that real time information can be weighted accordingly when factoring for this simultaneous bleaching behavior. Additional work must be performed to find more sensitive photospectroscopy techniques and equipment that can read the miniscule color changes that will occur at the low doses performed during proton RT.

References

[1] G. F. Knoll, Radiation Detection and Measurement, New Delhi: Wiley India Pvt. Ltd., 2010.

[2] A. Thompson and B. N. Tayler, "Guide for the Use of the International System of Units (SI) NIST Special Publication 811," 2008. [Online]. Available: https://www.nist.gov/pml/special-publication-811/nist-guide-si-chapter-5-units-outside-si. [Accessed 18 August 2018].

[3] L. A. DeWerd, L. Bartol and S. Davis, "Presentation, AAPM Summer School," 24 June 2009. [Online]. Available: https://www.aapm.org/meetings/09SS/documents/24DeWerd-TLDs.pdf. [Accessed 11 August 2018].

[4] H. Pick, "Color Centers in Alkali Halides," *Il Nuovo Cimento*, vol. 7, no. S2, pp. 498-522, 1958.

[5] P. Avakian and A. Smakula, "Color Centers in Cesium Halide Single Crystals," *Phys. Rev.*, vol. 120, no. 6, 2007.

[6] W. H. Duerig, "Color Centers Produced by X-Rays at Low Temperatures," *UMI Dissertation Publishing*, 1052.

[7] H. Hersh, "Color Centers in X-Rayed Potassium Iodide," *Phys. Rev.*, vol. 105, no. 5, pp. 1158-1167, 1956.

[8] I. Mador and et al., "Production and bleaching of color centers in x-rayed alkali halide crystals," *Phys. Rev.*, vol. 96, no. 3, p. 617, 1954.

[9] J. Markham, R. Platt and I. Mador, "Bleaching Properties of F Centers in KBr at 5K," *Phys. Rev.*, vol. 92, no. 3, pp. 597-603, 1953.

[10] W. L. McLaughlin, A. Miller, S. C. Ellis and A. C. Lucas, "Radiation-Induced Color Centers in LiF for Dosimetry at High Absorbed Dose Rates," *Nuclear Instruments and Methods*, vol. 175, pp. 17-18, 1980.

[11] F. Morehead and F. Daniels, "Thermoluminescence and Coloration of Lithium Flouride Produced by Alpha Particles, Electrons, Gamma Rays, and Neutrons," *The Journal of Chemial Physics*, vol. 27, 1957.

[12] D. Robinson and et al., "A study of the F-center in several alkali halides," 1967. [Online]. Available: Iowa State University Digital Repository. [Accessed 31 June 2017].

[13] F. Seitz, "Color Centers in Alkali Halide Crystals. II," *Reviews of Modern Physics*, vol. 26, no. 1, pp. 7-94, 1954.

[14] A. E. Hughes and D. Pooley, "High Dose Proton Irradiation of Alkali Halides," *Journal of Phsyics C: Solid State Physics*, vol. 4, pp. 1963-1976, 1971.

[15] M. Georgiev, "Two-electron F' centers in alkali halides: A negative-U analysis," [Online]. Available: https://arxiv.org/ftp/cond-mat/papers/0509/0509638.pdf. [Accessed 17 August 2018].

[16] N. X. Xinh, "Sidebands of the U-Center-Induced Infrared Absorption Spectra of Alkali-Halide Crystals*," *Physical Review*, vol. 163, no. 3, pp. 896-909, 1967.

[17] L. Brady, "The Changing Role of Radiation Oncology in Cancer Management," *Cancer*, vol. 51, pp. 2506-2514, 1983.

[18] R. E. Curtis, J. D. Boice, M. Stovall, L. Bernstein and e. al., "Risk of Leukemia After Chemotherapy and Radiation Treatment for Breast Cancer," *The England Journal of Medicine*, vol. 326, no. 26, pp. 1745-1751, 1992.

[19] D. E. Gerber and T. A. Chan, "Recent Advances in Radiation Therapy," *American Academy of Family Physicians*, vol. 78, no. 11~, pp. 1254-1262, 2008.

[20] J. Balter and e. al., "Uncertainties in CT-based radiation therapy treatment planning associated with patient breathing," *Intl. J. Rad. Oncology Bio. Phys.*, vol. 36, no. 1, p. 167, 1996.

[21] G. Chui, "Symmetry," 1 December 2008. [Online]. Available: https://www.symmetrymagazine.org/article/december-2008/the-power-of-proton-therapy. [Accessed 8th August 2018].

[22] J. Melody, A. T. Berman and N. Vapiwala, "The Evolution of Proton Beam Therapy: Insights From Early Trials and Tribulations," *International Journal of Radiation Oncology Biology Physics*, vol. 90, no. 4, pp. 733-735, 25 July 2014.

[23] M. A. Shampo, R. A. Kyle and D. P. Steensma, "Hans Geiger-German Physicist and the Geiger Counter," *Mayo Clin Proc.*, vol. 86, no. 12, p. e54, 2011.

[24] M. P. Short, C. A. Dennett, S. E. Ferry and R. Gupta, "Integrating Radiation Dosimetry". Massachusetts, United States of America Patent 62/233,377, 27 September 2015.

[25] C De Wagter, "The Ideal Dosimeter for Intensity Modulated Radiation Therapy (IMRT): What is Required?," *Journal of Physics: Conference Series*, vol. 3, pp. 4-8, 2004.

[26] I. A. E. A. N. D. Services, "Evaluated Nuclear Data File (ENDF) Database," 20 April 2018. [Online]. Available: https://www-nds.iaea.org/exfor/endf.htm. [Accessed 18 August 2018].

[27] M. Hernández-Ortiz and e. al., "Study of Afterglow and Thermoluminescence Properties of Synthetic Opal-C Nanoparticles for In Vivo Dosimetry Applications," in *MRS Proc.*, Cambridge University Press, 2013.

[28] T. Wilson, "Taylor's Nuke Site," no date. [Online]. Available: http://www.sciradioactive.com/radiation-effects/. [Accessed 18 August 2018].

[29] C. C. Bonato, H. B. Dias, M. d. S. Alves, L. O. Duarte, T. M. Dias, M. O. Dalenogare, C. C. B. Viegas and R. H. Elnecave, "In Vivo Dosimetry of Thryoid Doses from Different Irradiated Sites in Children and Adolescents: a Cross-Sectional Study," *Radiation Oncology*, vol. 9, no. 40, pp. 1-8, 2014.

[30] C. Aschan, "Applicability of Thermoluminescenct Dosimeters in X-Ray Organ Dose Determination and in the Dosimetry of Systemic and Boron Neutron Capture Radiotherapy," Academic Dissertation, University of Helsinki Report Series in Physics, Helsinki, Finland, 1999.

[31] T. Kron, M. Schneider, A. Murray and H. Mameghan, "Clinical Thermoluminescence Dosimetry: How do Expectations and Results Compare?," *Medical Dosimetry*, vol. 18, no. 3, p. 159, 1993.

[32] R. L. Harrison, "Introduction to Monte Carlo Simulation," in *AIP Conf Proc. Jan 5; 1204: 17-21*, 2010.

[33] S.-T. Chiu-Tsao, A. A. Melvin, P. T. Finger, D. S. Followill, A. S. Meigooni, C. S. Melhus, F. Mourtada, M. E. Napolitano, R. Nath, R. J. Mark, D. Rogers and R. M. Thomson, "Dosimetry of 125I and 103Pd COMSE Eye Plaques for Intraocular Tumors: Report of Task Group 128 by the AAPM and ABS," *Med. Phys.*, vol. 39, no. 10, pp. 6161-6184, 2012.

[34] J. J. DeMarco, T. D. Solber and J. B. Smathers, "A CT-Based Monte Carlo Simmulation Tool for Dosimetry Planning and Analysis," *Medical Physics*, vol. 25, no. 1, pp. 1-11, 1998.

[35] E. E. Fuhang, C. S. Chui, K. S. Kolbert, S. M. Larson and G. Sgouros, "Implementation of a Monte Carlo Dosimetry Method for Patient-Specific Internal Emitter Therapy," *Medical Physics*, vol. 24, no. 7, pp. 1163-1172, 1997.

[36] K. S. Kolbert, G. Sgouros, A. M. Scott, J. E. Bronstein, R. A. Malane, J. Zhang, H. Kalaigian, S. McNamera, L. Schwartzz and S. M. Larson, "Implementation and Evaluation of Patient-Specific Three-Dimensional Internal Dosimetry," *The Journal of Nuclear Medicine*, vol. 38, no. 2, pp. 301-308, 1997.

[37] J. Yang, J. Li, L. Chen, R. Price, S. McNeeley, L. Qin, L. Wang, W. Xiong and C.-M. Ma, "Dosimetric Verification of IMRT Treatment Planning Using Monte Carlo Simulation for Prostate Cancer," *Phsyics in Medicine & Biology*, vol. 50, pp. 869-878, 2005.

[38] W. P. Levin and e. al., "Proton beam therapy," *British J. Cancer*, vol. 93, no. 8, pp. 849-854, 2005.

[39] L. E. Antonuk, "Electornic Portal Imaging Devices: A Review and HIstorical Perspective of Contemporary Technologies and Research," *Physics in Medicine and Biology*, vol. 47, pp. R31-R65, 2002.

[40] M. G. Herman, J. M. Balter, D. A. Jaffray, K. P. McGee, P. Munro, S. Shalev, M. V. Herk and J. W. Wong, "Clinical Use of Electronic Portal Imaging: Report of AAPM Radiation Therapy Committee Task Group 58," *Med. Phys.*, vol. 28, no. 5, pp. 712-737, 2001.

[41] Y. D. Deene, "Essential Characteristics of Polymer Gel Dosimeters," *Journal of Physics: Conference Series*, vol. 3, pp. 34-57, 2004.

[42] C. Baldock, Y. D. Deene, S. Doran, G. Ibbott, A. Jirasek, M. Lepage, K. B. McAuley, M. Oldham and L. J. Schreiner, "Polymer Gel Dosimetry," *Phys. Med. Bio*, vol. 55, pp. R1-R63, 2010.

[43] L. J. Schreiner and T. Olding, *Gel Dosimetry*, Colorado College, CO, USA: presentation, AAPM 2009 Summer School, June 21-25, 2009.

[44] H. M. Swartz and e. al., "In Vivo EPR For Dosimetry," *Radiat Meas.*, vol. 42, no. 6-7, pp. 1-18, 2007.

[45] J.-J. Ahn, K. Akram, H.-K. Kim and J.-H. Kwon, "Electron Spin Resonance Spectroscopy for the Identification of Irradiated Foods with Complex ESR Signal," *Food Anal. Methods*, vol. 6, pp. 301-308, 20123.

[46] H. M. Swartz and e. al., "Electron Paramagnetic Resonance Dosimetry for a Large-Scale Radiation Incident," *Health Phys.*, vol. 103, no. 3, pp. 255-267, 2012.

[47] B. Nilsson, B.-I. Ruden and B. Sorcini, "Characteristics of Silicon Diodes as Patient Dosemeters in External Radiation Therap," *Radiotherapy and Oncology*, vol. 11, pp. 279-288, 1988.

[48] T. A. N. S. E. Portal, "Basic Radiation Detection," [Online]. Available: http://nsspi.tamu.edu/nsep/courses/basic-radiation-detection/semiconductor-detectors/introduction/introductionwww.aapm.org/meetings/09SS/documents/28Zhu-Diodes.pdf..

[49] G. Lutz, Semiconductor Radiation Detectors: Device Physics, New York City: Springer-Verlag Berlin Heidelberg, 1999, 2007.

[50] M. Essers and B. J. Mijnheer, "In Vivo Dosimetry During Exteranl Photon Beam Radiotherapy," *Int. J. Radiation Oncology Biol. Phys.*, vol. 43, no. 2, pp. 245-259, 1999.

[51] R. Ramaseshan, K. S. Kohli, T. J. Zhang, T. Lam, B. Norlinger, A. Hallil and M. Islam, "Performance Characteristics of a microMOSFET as an in Vivo Dosimeter in Radiation Therapy," *Institute of Physics Publishing - Physics in Medicine and Biology*, vol. 49, pp. 4031-4048, 2004.

[52] A. S. Beddart, T. R. Mackie and F. H. Attix, "Water-Equivalent Plastic Scintillation Detectors for High-Energy Beam Dosimetry: I. Physical Characteristics and Theoretical Considerations," *Phys. Med. Bio.*, vol. 37, no. 10, pp. 1883-1900, 1992.

[53] A. S. Beddart, T. R. Mackie and F. H. Attix, "Water-Equivalent Plastic Scintillation Detectors for High-Energy Beam Dosimetry: II. Properties and Measurements," *Phys. Med. Biol.*, vol. 37, no. 10, pp. 1901-1913, 1992.

[54] A. S. Beddar, N. Suchowerska and S. H. Law, "Plastic Scintillation Dosimetry for Radiation Therapy: Minimizing Capture of Cerenkov Radiation Noise," *Institute of Physics Publishing - Physics in Medicine and Biology*, vol. 49, pp. 783-790, 2004.

[55] S. Beddar, "Scintillation Dosimetry: Review, New Innovations and Applications," [Online]. Available: https://www.aapm.org/meetings/09ss/documents/32beddar-plasticdosimeters.pdf. [Accessed 23 August 2018].

[56] C.-H. Min, C. H. Kim and J.-W. K. Min-Young Youn, "Prompt Gamma Measurements for Locating the Dose Falloff Region in the Proton Therapy," *Applied Physics Letters*, vol. 89, pp. 183517-1 - 183517-3, 2006.

[57] J. C. Polf, D. Mackin, E. Lee, S. Avery and S. Beddar, "Detecting Prompt Gamma Emission During Proton Therapy: the Effects of Detector Size and Distance from the Patient," *Phys Med Biol.*, vol. 59, no. 9, pp. 2325-2340, 2014.

[58] P. Gueth, D. Dauvergne, N. Freud, J. M. Letang, C. Ray, E. Testa and D. Sarrut, "Machin Learning-Based Patient Specific Prompt-Gamma Dose Monitoring in Proton Therapy," *Phys. Med. Biol.*, vol. 58, pp. 4563-4577, 2013.

[59] M. Testa, C. H. Min, J. M. Verburg, J. Schumann, H.-M. Lu and H. Paganetti, "Range Verification of Passively Scattered Proton Beams Based on Prompt Gamma Time Patterns," *Institute of Physics and Engineering in Medicine - Physics in Medicine & Biology*, vol. 59, pp. 4181-4195, 2014.

[60] J. M. Verburg and J. Seco, "Proton Range Verification Through Prompt Gamma-Ray Spectroscopy," *Institute of Physics and Engineering in Medicine - Physics in Medicine & Biology*, vol. 59, pp. 7089-7106, 2014.

[61] P. G. Ortega, I. Torres-Espallardo, T. T. Bohlen, F. Cerutti, M. P. W. Chin, A. Ferrari, J. E. Gillam, C. Lacasta, G. Llosa, J. Oliver, M. Rafecas, P. R. Sala and P. Solevi, "Noise Evaluation of Prompt-Gamma Technique for Proton-Therapy Range Verification Using a Compton Camera," *Nucl. Sci. Symp. Med. Imaging Conf. (NSS/MIC), IEEE*, pp. 1-7, 2013.

[62] A. Knopf, K. Parodi, T. Bortfeld, H. A. Shih and H. Paganetti, "Systematic Analysis of Biological and Physical Limitations of Proton Beam Range Verification With Offline PET/CT Scans," *IOP Publishing - Physics in Medicine and Biology*, vol. 54, pp. 4477-4495, 2009.

[63] C. W. Scarantino, D. M. Ruslander, C. J. Rini, G. G. Mann, H. T. Nagle and R. D. Black, "An Implatable Radiation Dosimeter for Use in External Beam Radiation Therapy," *Med. Phys.*, vol. 31, no. 9, pp. 2658-2671, 2004.

[64] K. V. Rao, "Colour Centre PHenomena in Alkali Halide Crystals X-Ray-Irradiated Under High Electric Fields," *Nuclear Tracks and Radiation Measurments*, vol. 10, no. 1-2, pp. 203-214, 1985.

[65] D. Pooley, "The Saturation of F-Centre Production in Alkali Halides Under Proton Irradiation," *British Journal of Applied Physics*, vol. 17, pp. 855-861, 1966.

[66] A. E. Hughes and D. Pooley, "High Dose Proton Irradiation of Alkali Halides," *J. Phys. C: Solid St. Phys.*, vol. 4, pp. 1963-1976, 1971.

[67] H. N. Hersh, "Studies of Color Centers in Polycrystalline Compressed Pellets of Alkali Halides*," *The Journal of Chemical Physics*, vol. 27, no. 6, pp. 1330-1338, 1957.

[68] M. Piccinini, F. Ambrosini, A. Ampollini, M. Carpanses, L. Picardi, C. Ronsivalle, F. Bonfili, S. Libera, M. A. Vincenti and R. M. Montereali, "Optica Spectroscopy and Imaging of Colour Centres in Lithium Fluoride Crystals and Thin Films irradiated by 3MeV Proton Beams," *Nuclear Instruments and Methods in Physics Research B*, vol. 326, pp. 72-75, 2014.

[69] W. L. McLaughlin, A. C. Luca, B. M. Kapsar and A. Miller, "Electron and Gamma-Ray Dosimetry Using Radiation-Induced Color Centers in LiF," *Radiat. Phys. Chem.*, vol. 14, pp. 468-480, 1979.

[70] J. P. Grutters, A. G. Kessels, M. Pijls-Johannesma and D. D. Ruysscher, "Comparison of the effectiveness of radiotherapy with photons, protons and carbon-ions for non-small cell lung cancer: A meta-analysis," *In Radiotherapy and Oncology*, vol. 95, no. 1, pp. 32-40, 2010.

[71] E. A. Pearlstein, "Change of Electrical Conductivity of Sodium Chloride upon Bombardment with High-Energy Protons*," *Phys. Rev.*, vol. 92, no. 4, pp. 881-882, 1953.

[72] H. Paganetti and P. van Luijk, "Biological Considerations when comparing proton therapy with photon therapy," *Seminars in Radiation Oncology*, vol. 23, no. 2, 2013.